Strange Hadron Production as a Function of Multiplicity and Transverse Spherocity in proton-proton Collisions at $\sqrt{s} = 13$ TeV

Maria Mårtenson

Thesis Submitted for Degree of Master of Science

Project Duration: 8 Months

Supervised by David Silvermyr

LUND
UNIVERSITY

Department of Physics
Division of Particle Physics
January 2018

Abstract

This thesis presents the study of the K^0_s, Λ, and $\bar{\Lambda}$ production in pp collisions at $\sqrt{s} = 13$ TeV recorded by the ALICE experiment at the LHC. The K^0_s, Λ, and $\bar{\Lambda}$ particles are reconstructed in the transverse momentum (p_{T}) range of $1.0 - 12.0\,\mathrm{GeV}/c$ by using their V^0 topology. The p_{T}-spectra are studied as a function of the charged-particle multiplicity and the transverse spherocity. The identified particle productions are studied for events including all multiplicity classes (V0M:0-100%) and for high multiplicity events (V0M.0-10%). Further, the event shape analysis using the transverse spherocity includes two selections of the high multiplicity events, low spherocity events ($S_O < 0.47$) and high spherocity events ($S_O > 0.76$). The baryon-to-meson ratio $(\Lambda + \bar{\Lambda})/2K^0_s$ as a function of the transverse momentum is studied for the four event selections. The results exhibit an enhanced production of K^0_s, Λ, and $\bar{\Lambda}$ particles and an enhanced baryon-to-meson ratio in the intermediate transverse momentum region for the high spherocity events ($S_O > 0.76$) compared to the other three event selections.

Populärvetenskaplig Sammanfattning

Partikelfysik studerar materians minsta byggstenar och hur de växelverkar med varandra. De partiklar som bygger upp all observerad materia kallas kvarkar och leptoner. Dessa partiklar växelverkar med varandra genom att överföra diskreta mängder energier. Transaktionen av energi sker genom att utbyta en partikel som kallas boson. De kraftöverförande boson-partiklarna, kvarkarna och leptonerna är alla inkluderade i den grundläggande teorin inom partikelfysik som heter Standardmodellen.

Kvarkar är bundna i tillstånd om två och tre genom den starka kraften, som verkar genom att utbyta den boson-sort som heter gluon. Dessa bundna tillstånd kallas hadroner och de mest välkända hadronerna är förmodligen protonen och neutronen. Tillsammans med elektroner, bygger protoner och neutron upp all materia runt omkring oss, det vill säga gaser, vätskor och fasta former.

Studien som presenteras i den här uppsatsen handlar om ett materietillstånd som inte existerar under normala förhållanden utan kan endast produceras i laboratoriemiljö. Detta tillstånd som kallas *Kvark-Gluon-Plamsa* kräver extremt höga temperaturer och densiteter för att bildas. En sådan extrem miljö kan skapas vid världens största partikelaccelerator Large Hadron Collider (LHC) vid CERN i Schweiz. Där accelereras bland annat tunga blykärnor upp till över 99% av ljusets hastighet för att sedan kollidera. När blykärnorna kolliderar skapas en extremt varm och tät miljö där Kvark-Gluon-Plasman kan bildas. Plasman existerar bara i ett ögonblick och kan således inte studeras under den tid då den existerar. I stället är det de partiklarna som detekteras efter kollisionen som används när plasmans existens och egenskaper fastställs.

Att Kvark-Gluon-Plasma bildas genom att kollidera tunga kärnor (tungjonskollisioner) i ultra-relativistiska hastigheter bevisades i början på 2000-talet. Historiskt sett så har kollisioner av lättare partiklar, som proton-proton kollisioner, använts som referens när plasmans egenskaper har fastställts. Men under senare år har forskning visat att proton-proton kollisioner, i vilka många nya partiklar har bildats, genererar fenomen som påminner om Kvark-Gluon-Plasmans kännetecken.

I den här uppsatsen studeras protonkollisioner, detekterade av ALICE detektorn vid LHC, i ett försök att obervera några av de signaler som Kvark-Gluon-Plasman ger upphov till. Tre typer av hadroner, Λ och dess antipartikel $\bar{\Lambda}$, samt K^0_s analyseras och de är av intresse då de innehåller varsin s-kvark (samt andra lättare kvarkar). Den här kvark-sorten finns inte innan kollisionen, då endast u-och d-kvarkar bygger upp protoner. Alla s-kvarkar är således skapade i kollisionen eller strax efter. I tungjonskollisioner där Kvark-Gluon-Plasman bildats har ett överflöd av hadroner som innehåller s-kvarkar observerats och av den anledningen undersöks partikelproduktionen av just Λ, $\bar{\Lambda}$ och K^0_s i den här analysen.

Acknowledgements

First and foremost, I would like to thank my supervisor David Silvermyr for his support and feedback. I would like to give many thanks to the ALICE group at Lund University; Peter Christiansen, Vytautas Vislavičius, Martin Ljunggren, Tuva Richert, Jonatan Adolfsson, and Evert Stenlund. A special thanks to Anders Oskarsson for thoroughly proofreading my thesis.

A big thanks to the ALICE master students Madeleine Sjögren, Adam Benny Johansson, Rickard Lydahl, and Adrian Nassirpour. Lastly, many thanks to everyone at the Lund Particle Physics division.

Contents

List of Acronyms

ALICE A Large Ion Collider Experiment

CERN Conseil Européen pour la Recherche Nucléaire

ITS Inner Tracking System

LHC Large Hadron Collider

RHIC Relativistic Heavy-Ion Collider

SDD Silicon Drift Detector

SM Standard Model

SPD Silicon Pixel Detector

SPS Super Proton Synchrotron

SSD Silicon Strip Detector

TPC Time Projection Chamber

QCD Quantum Chromodynamics

QED Quantum Electrodynamics

QFT Quantum Field Theory

QGP Quark-Gluon Plasma

1 Introduction

Particle physics aims to describe the smallest building blocks of matter and how they interact. Our current understanding of the fundamental constituents of the Universe is embodied in the Standard Model of particle physics. The theory describes, with the exception for gravity, the fundamental particles and their interactions. However, which particles are considered to be fundamental have changed over time. In 1964, Murray Gell-Mann and George Zweig independently proposed the existence of quarks. At the time, several different types of strongly interacting particles called hadrons had been discovered and among many particle physicists, they were believed to be to some extent elementary [1]. Gell-Mann and Zweig postulated that hadrons are not elementary particles, but instead compositions of quarks[1]. The first experimental evidence for quarks was announced in 1968 and by the end of 1979, after the mediator of the strong force called the gluon had been discovered, there were hardly any doubts that hadrons were compositions of quarks bound together by the gluons. The two types of hadrons known as the proton and the neutron, together with the electron, constitute the matter in the low-energy Universe, i.e. solids, liquids, and gases.

The quarks and gluons are confined within hadrons by their color charges, which is the quantum number characterizing the strong force. However, in the 1970s, theoretical consideration led to the beliefs that a new state of matter, where the quarks and gluons are deconfined, could be produced in a laboratory environment by colliding heavy nuclei at extremely high energies [2]. The first circumstantial evidence for this matter, called quark-gluon plasma (QGP), being created in heavy-ion collisions was announced in the year 2000. Collisions of lead nuclei recorded at the Super Proton Synchrotron (SPS) accelerator at CERN (Conseil Européen pour la Recherche Nucléaire) had demonstrated QGP signatures. The existence of the QGP in heavy-ion collisions was validated in 2005 by the study of gold-gold (Au-Au) collisions at the Relativistic Heavy Ion Collider (RHIC) at Brookhaven National Laboratory [3].

Historically, the QGP has been considered to be a heavy-ion phenomenon and the smaller systems produced in proton-proton (pp) or proton-nucleus collisions have been a baseline when establishing the QGP signatures. However, research over the past decade indicates that something reminiscent of the QGP is created in small systems as well [4, 5, 6]. In this thesis, pp collisions recorded by the ALICE detector at the Large Hadron Collider (LHC), CERN, are analyzed in the search for heavy-ion like phenomena in small systems.

1.1 Aim of the Thesis

The QGP is a transient phase and it only exists $\sim 10^{-22}$ s when created in heavy-ion collisions [7]. Therefore, the QGP cannot be studied directly but instead, is manifested through observable signatures that characterize the outcome of the detected particles. One of the first signatures to be proposed was strangeness enhancement, an abundance of hadrons consisting of one or more strange quarks is expected in heavy-ion collisions if the QGP phase is created. Further, signatures as enhanced baryon-to-meson ratio, collective flow, heavy-quark suppression, and jet quenching are expected

[1] Zweig referred to them as "aces".

as well in heavy-ion collisions. The small systems produced in pp collisions cannot be expected to generate these signatures to the same extent as in heavy-ion collisions. The system of two protons is not directly comparable to a large system such as those produced when colliding two lead nuclei, which in the initial state contains of 164 protons and 252 neutrons.

The aim of this thesis is to first identify and reconstruct three types of hadrons, which all consist of one strange quark each (along with other lighter quarks). The three hadrons treated are two baryons Λ and $\bar{\Lambda}$, and the meson K^0_s. The reconstructed hadron yields will be measured for collisions required to have at least one inelastic scattering and then compared to the yields for collisions in which a large number of particles are produced, i.e. high multiplicity events. The system of particles in high multiplicity pp events are more similar to those in heavy-ion collisions and QGP-like features might be more pronounced in these events. Finally, to further investigate heavy-ion like phenomena in small systems, the high multiplicity events will be used for an event shape analysis. By the transverse spherocity, events giving rise to an evenly distributed particle production in momentum space will be selected and compared to events in which the particle distributions are less even. By the four different event selections, the aim is to study the event multiplicity and event shape dependence of the identified particle production.

In Chapter 2 and 3, the Standard Model and the high-energy physics phenomenology are introduced. Chapter 4 gives an overview of the ALICE experiment at the LHC. The analysis performed in this thesis is described in Chapter 5 followed by the results and discussion in Chapter 6 and 7, respectively. Finally, conclusions and an outlook are given in Chapter 8.

2 The Standard Model

The Standard Model (SM) is a Quantum Field Theory (QFT) and it provides a mathematical description of the *elementary particles* and the *interactions* between them. The elementary particles, which are particles with no known internal structure, are treated as excited states of their corresponding underlying quantum fields. They interact by exchanging field quanta in the form of force mediating particles. The elementary particles treated in the SM are the *fermions* and the *bosons*, and their properties are determined by a combination of quantum numbers such as spin, charges and masses [8]. Fermions are the "matter particles" in the SM and the interactions between the fermions are mediated by the bosons. Fermions and bosons will be further discussed in Section 2.2.

The four fundamental forces, through which the elementary particles interact, are the strong force, the weak force, electromagnetic force and gravitational force. The latter is not included in the SM since there is not yet a complete QFT for gravity. However, the effect of the gravitational force can be neglected when considering the minuscule scale of fundamental particles and their interactions[2] [8]. The other three fundamental

[2]The strength of gravity relative to the strong force is of the order 10^{-39}, where the strength of the strong force being equal to 1 on the scale of two interacting fundamental particles at a distance corresponding to the radius of a proton (1 fm=10^{-15} m)[8].

forces are successfully described by QFT and are thus a part of the SM.

The SM was elaborated into its final form during the 1970s and it has since then been in agreement with almost all current experimental data. Through its success, it has come to be an established theory for particle physics [1].

2.1 The Theoretical Framework

The SM is a QFT in which the elementary particles are treated as field quanta of underlying quantum fields. Consider electromagnetic interactions, which are described by the QFT of quantum electrodynamics (QED). These interactions take place between electrically charged fermions and are mediated by the boson known as the photon. A well known electrically charged fermion is the electron. In an interaction between an electron and a photon, the electron is represented as a quantum state of a fermion field, while the photon is the quantum state of an electromagnetic field. Hence, the interaction between these two particles is an interaction between two fields that couples to the same charge (quantum number).

The dynamics of the fields and their quantum states are formulated and determined by the Lagrangian density $\mathcal{L}$ (Lagrangian for short), which is a function of the fields. The Lagrangian comprises the potential energy parts, which specify the forces, often called the interaction Lagrangian. Furthermore, it contains kinetic energy parts that solely depend on the spins of the particles [9].

An essential part of the theoretical framework of SM is Feynman diagrams. Feynman diagrams represent the sum of the possible time-orderings where an interaction process can occur [8]. A fermion-boson interaction is visualized by the Feynman diagrams in Figure 2.1.1. There are initially two fermions a and b that interact by exchanging a virtual boson X and this leads to the final state of the two fermions c and d. A virtual particle represents the intermediate state in the Feynamn diagram and it is impossible to know exactly how this state will happen. Either fermion a emits the boson X that is absorbed by b, or vice versa. Therefore, the Feynman diagram of the scattering process ($a + b \rightarrow c + d$) in Figure 2.1.1 is the sum of the two lowest time-ordering diagrams, which represent the intermediate states. The Feynman diagrams are more than visual representations of interaction processes, they are the basis when calculating QFT processes using perturbation theory. The diagrams conform to certain Feynman rules that depend on the interaction Lagrangian. Each vertex, which is the point representing the interaction, is associated to a coupling constant, which is determined by the fundamental interaction being considered. The coupling constant most relevant to this thesis is the strong coupling constant and it will be discussed in Section 2.3.1.

Finally, the SM is a gauge theory, which ensures regulation of redundant degrees of freedom in the Lagrangian and implies that the Lagrangian is invariant under local gauge transformations [9]. The transformations form symmetry groups (gauge groups) of the theory and these symmetry groups are the basis for the fields in the SM. The electromagnetic force and weak force are unified by the Glashow-Salam-Weinberg (GSW) theory and the fields are based on the $U(1) \times U(2)$ symmetry group, while the theory describing strong interactions, Quantum Chromodynamics (QCD), is based on the $U(3)$ symmetry group. There are associated group generators for

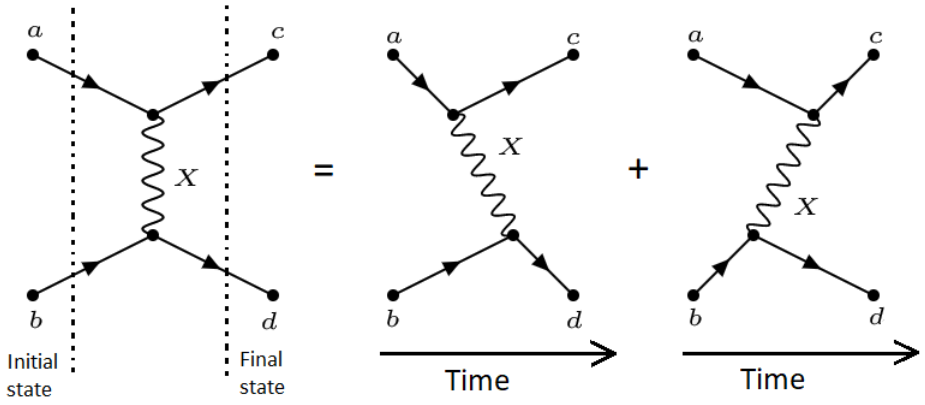

Figure 2.1.1: The left Feynman diagram of the scattering process $a + b \rightarrow c + d$ represents the sum of the two possible time-ordered diagrams to the right.

each symmetry group, which generate corresponding vector fields (or gauge fields). The quanta of these vector fields are the fundamental particles called gauge bosons (vector bosons). The two theories GSW and QCD construct the QFT of the SM, and from the $U(1) \times U(2) \times U(3)$ groups arise 1+3+8=12 generators, which in turn correspond to the 12 force mediating gauge bosons in the SM. The GSW and the QCD are non-Abelian gauge theories, which gives rise to the property of self-interacting gauge bosons. The QED, which is separated from the unified theory GSW, is an Abelian theory and thus, the photons do not self-interact. The self-interaction of gauge bosons in the QCD and its impact will be discussed in Section 2.3. The Feynman rules, the Lagrangian and gauge theory will not be explained any further since it is beyond the scope of this thesis, for a more elaborate theoretical description of the SM see Reference [8, 9].

2.2 The Fundamental Particles and Forces

Fermions are the constituents of matter, and all the known matter in the Universe appears to be made of these particles [8]. The electron, the electron neutrino, the up-quark and the down-quark are four fermions that are collectively referred to as the *first generation*. All matter in the low-energy Universe, such as solids, liquids, and gases, are constructed by the two quarks and the electron from the first generation. In addition to the four fermions of the first generation, there are two more generations of fermions, the *second* and *third generation*. The fermions of the second and third generation have exactly the same properties as their corresponding fermions from the first generation with an exception for the masses, which increase for each generation.

The Dirac equation of relativistic quantum mechanics describes the dynamics, such as intrinsic spin and magnetic moment, for each one of the fermions [10]. Fermions (and bosons) possess an intrinsic angular momentum called *spin*, which is one of the quantum numbers assigned to the particles in the SM. Fermions have a spin of the magnitude $\frac{1}{2}$ and thus, they obey the Pauli exclusion principle [8]. This means that two identical fermions, i.e. having identical quantum numbers, cannot occupy the same quantum state simultaneously. Furthermore, the Dirac equation shows that there ex-

Table 2.2.1: The spin-$\frac{1}{2}$ fermions of the Standard Model. The three generations of quarks and leptons are presented in the table, along with their corresponding masses and charges. The values of the charges and masses are expressed in natural units with c=$\hbar$=1 and given by the Particle Data Group [11].

Generation	Quarks			Leptons		
	Particle	Mass	Charge [e]	Particle	Mass	Charge [e]
I	Up (u)	2.2 MeV	+2/3	Electron (e)	0.511 MeV	-1
	Down (d)	4.7 MeV	-1/3	Electron Neutrino (ν_e)	<2.2 eV	0
II	Charm (c)	1.28 GeV	+2/3	Muon (μ)	106 MeV	-1
	Strange (s)	96 MeV	-1/3	Muon Neutrino (ν_μ)	<0.17 MeV	0
III	Top (t)	173 GeV	+2/3	Tau (τ)	1.78 GeV	-1
	Bottom (b)	4.18 GeV	-1/3	Tau Neutrino (ν_τ)	<11.5 MeV	0

ists an antiparticle state, which has the same mass but with opposite charges, for each of the twelve fundamental fermions in the SM. To distinguish the symbols for antiparticles from the symbols of their corresponding particles, either a bar is placed over the particle symbol or the antiparticle is denoted with its charge.

Fermions interact with each other through the fundamental forces and they are divided into two different subgroups of six, *quarks* and *leptons*, depending on the forces they can experience [8]. All the fermions can undergo weak interactions. Both quarks and leptons can interact electromagnetically with the exception for the three electrically neutral neutrinos. The six quarks are the only fermions that can interact strongly and this is due to them possessing the quantum number called *color*, which will be discussed more thoroughly in Section 2.3. The electron, muon, tau-lepton and their associated neutrinos, the electron neutrino, mu-neutrino and tau-neutrino, all belong to the subgroup of fermions that are collectively referred to as leptons. All the different types, also called *flavors*, of quarks and leptons and their corresponding masses[3] and electrical charges are presented in Table 2.2.1.

Each one of the fundamental interactions in the SM are mediated by gauge bosons that are transferring four-momentum between particles. The gauge bosons have a spin of the magnitude 1 and thus, do not have to obey the Pauli exclusion principle. Therefore, it is possible for bosons to occupy the same quantum state. A list of the spin-1 bosons in the SM and which of the elementary particles they act on is presented in

[3]The quark masses presented in Table 2.2.1 are the *bare* quark masses (also called the current masses). The bare quark masses are the masses of asymptotically free quarks, while quarks in bound (colorless) states have the heavier *constituent* masses.

Table 2.2.2: The spin-1 bosons of the Standard Model are presented in the table. The charges and masses are expressed in natural units with c=$\hbar$=1 and given by the Particle Data Group [11].

Force	Boson	Interact with	Mass [GeV]	Charge [e]
Strong	Gluon (g)	Color charged particles	0	0
Electromagnetic	Photon (γ)	Electrically charged particles	0	0
Weak	$W^{\pm}$, Z^0	All fermions, electroweak gauge bosons	80.4, 91.2	$\pm$1, 0

Table. 2.2.2.

The gauge boson associated with the QED is the massless photon, which acts on all electrically charged particles. The weak force can be mediated by three different bosons, depending on the type of interaction. The weak charge-current interaction, which for example gives rise to the neutron β-decay ($n \rightarrow pe\bar{\nu}$), is mediated by the massive electrically charged W^- and W^+ bosons. The weak neutral-current interaction is mediated by the massive electrically neutral Z^0 boson. A distinguishing characteristic of the weak force is the possibility for fermions to change flavors when interacting weakly [8]. The weak force and its assigned quantum number *weak isospin* T_3 will be discussed in Section 2.4. The third force in the SM, the strong force, is described by the QFT named quantum chromodynamics (QCD). The force-mediators of the QCD are eight massless bosons called gluons that couple to the quantum number color charge. The QCD will be elaborated further in Section 2.3.

The final elementary particle in the SM is the massive Higgs boson H^0. Unlike the force-mediating spin-1 vector bosons in the SM, the H^0 boson is a spin-0 scalar boson. The Universe is assumed to be filled with a Higgs field that has a non-zero value in vacuum. The H^0 boson is an excited state of the Higgs field that generates mass through electroweak spontaneous symmetry breaking, known as the Higgs mechanism. It is the symmetry of the $SU(1)$ and $SU(2)$ groups that are effectively broken and by this, the weak gauge bosons acquire mass but the photon remains massless [9]. The Higgs field does not interact with color fields, which means that the gluons also remain massless. The initially massless fermions interact with the Higgs field, since all fermions can interact either weakly or electromagnetically, and by this they acquire their masses. The currently known mass of the H^0 boson is 125.09 GeV [11] and it gets its mass by interacting with the Higgs field.

2.3 Quantum Chromodynamics

Quantum Chromodynamics (QCD) is the quantum field theory that describes strong interactions in the Standard Model. As mentioned in the previous section, the QCD interactions are mediated by massless spin-1 gluons to which only color charged particles couple. Quarks are the only fermions carrying color charge and the three conserved color charges in QCD are red (r), blue (b), and green (g). Quarks can carry one of these charges, while the antiquarks carry the opposite color charges $\bar{r}$, $\bar{b}$, and $\bar{g}$. In order for the color to be conserved in interactions, the gluons themselves must carry a combination of color and anticolor charges [8]. The three color and the three anticolor charges can be combined into eight different colored states, which correspond to eight physical gluons. The property of gluons themselves carrying color charges leads to self-interaction among gluons and this in turn gives rise to important properties of the QCD, namely *color confinement* and *asymptotic freedom*.

The QCD Lagrangian cannot be solved analytically [12]. However, it can be solved using perturbation theory in the high-momentum regime. This regime corresponds to a distance much smaller than the radius of a proton, which is of the order 1 fm $\sim$ 200 MeV^{-1}. In the high-momentum regime, the perturbative calculations show that the color charged particles are asymptotically free when probed at a short distance. In the low-momentum regime, the expansion of the QCD Lagrangian does not converge rapidly and the perturbative approach fails, leading to the hypothesis of confinement. The dependence of the momentum (energy) scale at which a physical process occurs divides the QCD into two categories, non-perturbative and perturbative. The non-perturbative (soft) QCD processes correspond to interactions with low-momentum transfer, whereas the perturbative (hard) QCD processes correspond to interactions with high-momentum transfer.

2.3.1 Asymptotic Freedom and the Strong Coupling Constant

The interaction strength between particles in the SM is determined by a dimensionless coupling constant. Each of the three forces has an associated coupling constant and despite the name, they are not constants. The values of the running coupling constants vary depending on the momentum q being transferred in the interactions.

The coupling constant of the QCD, denoted as α_s, decreases with increasing momentum transfer $|Q^2|$. Qualitatively, the running of α_s can be explained by the phenomena of *screening* and *antiscreening*. Consider the scattering process similar to the one showed in Figure 2.1.1, but with two initial-state quarks q_1 and q_2 interacting by one-gluon exchange, giving rise to their final states q_1' and q_2'. If q_1 emits a virtual gluon, there is a probability that the emitted gluon fluctuates into a quark-anitquark pair before getting absorbed by q_2. This quantum fluctuation in the form of a *fermion loop* gives rise to a vacuum polarization effect that generates a field in the opposite direction of q_1. Consequently, the total net field of q_1 (and q_2) will be smaller. The antiscreening effect arises when the emitted gluon self-interacts by fluctuating into a gluon loop before getting absorbed. This *bosonic loop*, unlike the fermions loop, enhances the color field of q_1 (and q_2). There are infinite contributions from loop diagrams when considering a quark-quark scattering process. However, these infinites

can be eliminated through a process called renormalization. When considering the two lowest-order vacuum polarization effects, which are shown in Figure 2.3.1, the bosonic loop contributes more to the scattering process than the fermion loop [9]. This is due to there being eight gluons contributing to the bosonic loop, compared to the six quarks contributing to the fermion loop. In addition to that, the gluons have a larger color charge than the quarks.

As a consequence of the antiscreening effect being dominant, the quarks are surrounded by large color fields arising from self-interacting virtual gluons. To avoid these large color fields, one would have to probe the quarks at very short distances. If the distance is small enough, or equally the momentum transfer Q large enough, the effect of virtual gluons self-interacting can no longer be observed and the quark being probed will act as a quasi-free particle [8]. This property is called asymptotic freedom.

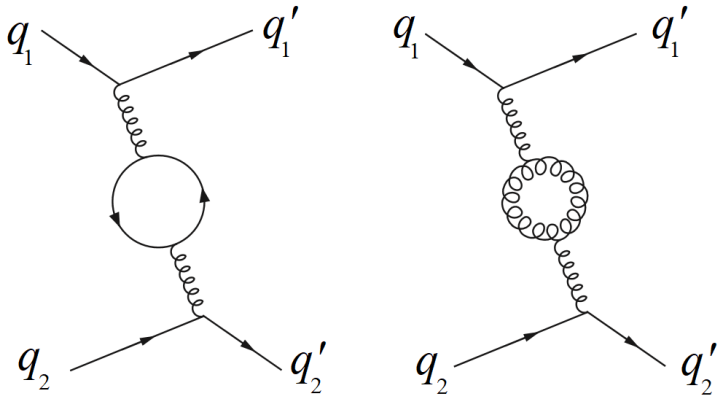

Figure 2.3.1: In a quark-quark scattering process involving a one-gluon exchange, the two lowest-order vacuum polarization corrections emerge from the fermion loop (left) and the bosonic loop (right).

At large momentum transfer, where quarks can be treated as quasi-free particles, the evolution of $\alpha(Q^2)$ is

$$\alpha_s(Q^2) = \frac{\alpha_s(\mu^2)}{1 + \beta_0 \alpha_s(\mu^2) \ln\left(\frac{Q^2}{\mu^2}\right)} \tag{2.3.1}$$

where $\beta_0 = \frac{1}{12\pi}(11N_c - 2N_f)$ accounts for the quark and gluon loops. The term with the number of colors N_c originates from the dominating gluon loops, which gives a positive contribution to the color field, while the term with the number of quark flavors N_f originates from the quarks loops, which gives a negative contribution. Since there are $N_c = 3$ colors and $N_f = 6$ quarks flavors, β_0 is greater than zero and α_s will decrease with increasing Q^2. The value of $\alpha(\mu^2)$ is determined at a chosen reference value μ, which is usually taken to be the mass of the Z boson [10].

When considering the energy range relevant to particle physics, the coupling constant of the QCD $\alpha_s(Q^2)$ varies significantly. At the energy scale of $\mid Q \mid \lesssim 1$ GeV, α_s is so strong that perturbative calculations cannot be used and instead, the hypothesis of color confinement is applied. This will be discussed in the next section. At the energy scale typical for modern high-energy collider experiments, $\mid Q \mid > 100$ GeV, α_s becomes sufficiently small that perturbation theory can be applied on QCD processes. When being probed by energies in this regime[4], quarks behave as essentially free particles.

[4]This energy regime corresponds to a distance scale a 100 times smaller than the radius of a proton.

2.3.2 Color Confinement and Hadronic States

The non-emergence of free quarks in experiments has lead to the hypothesis of color confinement. It states that color charged objects cannot propagate as free particles and consequently, it requires that a system of color charged particles can only be observed in a colorless (zero total color charge) state. Color confinement has not yet been proven analytically but it is believed to emerge from the gluon self-interactions. Qualitatively, the phenomena can be understood by considering the separation of a quark and an antiquark (which have an attractive strong force between them). The quark and the antiquark interact by exchanging virtual gluons and in turn, these virtual gluons interact with each other due to carrying color charge themselves. This creates an attractive color field between the two quarks that acts as an effective potential on the form $V(\mathbf{r}) \sim \kappa r$, where the value of $\kappa \sim$1 GeV/fm has been determined experimentally [8]. This potential will grow linearly with distance r leading to an infinite amount of work is required to completely separate the quarks.

Color charged particles being unable to propagate as free particles means that they can only be probed via colorless states. These colorless states are called *hadrons* and the most commonly known hadron is the proton, which is also the only stable hadron. Unstable hadrons will decay via the strong force if it is possible and these types of decays occur on a time scale of $\sim 10^{-23}$ s. If it is not possible for the hadron to decay strongly (which depends on the properties of the hadron), it will decay either electromagnetically or weakly. The electromagnetic and weak decays occur on a time scale of $\sim 10^{-20}$ and $\sim 10^{-15}$ to 880 s, respectively [11].

The hadrons are compositions of valence quarks and virtual gluons that give rise to quark-antiquark pairs production. The properties of the hadrons are determined by their valence quarks and these quarks can form two kinds of hadronic colorless states, *baryons* and *mesons*. Baryons consist of three quarks (qqq) and antibaryons three antiquarks ($\bar{q}\bar{q}\bar{q}$), while mesons consist of a quark and an antiquark ($\mathrm{q\bar{q}}$). Every hadron has a strictly conserved baryon (quantum) number $B = (n_q - n_{\bar{q}})/3$, where n_q is the number of quarks and $n_{\bar{q}}$ is the number of antiquarks. Accordingly, the baryons, antibaryons, and mesons have the baryon numbers +1, -1, and 0, respectively [9].

2.3.3 Quark-Gluon Plasma in the QCD

Quark-Gluon Plamsa (QGP) is a state of strongly interacting matter that exists at extremely high temperatures and densities. In ordinary (low-energy) conditions, quarks and gluons, which are collectivity referred to as partons, are confined in hadrons. However, at high temperatures or particle densities, the hadrons effectively dissolve and the partons become *deconfined*.

An important property to describe mobile charges in a electromagnetic (EM) plasma is the Debye screening length λ_D, which is the inverse of the Debye screening mass m_D. The mobile charges in a volume will be increasingly screened with each Debye length and the potential between them will decrease exponentially. Analogically, the asymptotically free color charged partons in the QGP can be thought of as the mobile charges in the EM plasma. The high temperature in the QGP state leads to a large production of quark-antiquark pairs and this in turn generates a very dense environment. In this environment, the λ_D will decrease to the point where it is less

than the radius of a hadron r_h. Hence, the partons of a specific hadron h_1 in the QGP system will find, at a distance less than r_h, color charged partons that are not of the original hadron composition. These new color charges will effectively screen the color field between the partons of h_1. Hence, the partons in h_1 will no longer be able to identify each other since the color field between them decreases by the screening. The hadronic compositions will be dissolved into a plasma and consequently, the quarks and gluons can move as free particles in the plasma volume since they are no longer confined to a local region [12].

The QGP is believed to have existed during the first few microseconds after the Big Bang when the universe was extremely hot[13]. In the present day, the QGP may exist at the center of neutron stars. The relatively low temperature of neutron stars will not generate a large production of quark-antiquarks pair. However, the extreme density of these star centers will compress the quarks to the point where $r_h < \lambda_D$.

The high temperature and density conditions needed to create the QGP state can be achieved at modern high-energy heavy-ion collider experiments. The phase transition from hadronic matter to the QGP matter occur at a critical temperature of $T_C \simeq 160$ MeV and an energy density of $\epsilon \simeq 1$ GeV/fm^3 [3]. The lifetime of the QGP created in heavy-ion collisions is short. After only about 10^{-22} s, the partons start to hadronize [7], meaning that they will start to combine with each other and once again be confined within hadrons. The short lifetime of the QGP makes it impossible to study the phenomenon directly and instead, the QGP manifests itself through different observable characteristics in the final-state particles. The observables of the QGP will be discussed in Section 3.2.

2.4 Weak Hadronic Interactions

The weak interaction is unique in the aspect that it is the only type of interaction in which the flavor of quarks and leptons can be changed. The quantum number describing the weak interactions is the *weak isospin* T_3, which is one of the components of the weak hypercharge Y [8]. The weak and electromagnetic interactions are unified by the weak hypercharge, which is identified as a linear combination of the electric charge Q and the weak isospin, $Y = 2(Q - T_3)$. The (left-handed[5]) up-type (u, c, t) and down-type (d, s, b) quarks have $T_3 = +\frac{1}{2}$ and $T_3 = -\frac{1}{2}$, respectively. A quark never transforms into another quark with weak isospin of the same sign. Hence, the up-type quarks transform into down-type quarks, and vice versa.

The weak interactions are mediated by the $W^{\pm}$ bosons and the Z^0 boson. The W^+ boson has $T_3 = +1$ and is emitted when a up-type quark (down-type antiquark) transforms into down-type quark (up-type antiquark). The W^- boson with $T_3 = -1$ is emitted when down-type quarks (up-down antiquark) transform into up-type quarks (down-type antiquark). The Z^0 has $T_3 = 0$ and leaves the flavors of the interacting particles unaffected.

[5]Only left-handed (right-handed) up-type and down-type quarks (antiquarks) are considered in this thesis. Right-handed quarks and left-handed antiquarks have weak isospin $T_3 = 0$ and do not undergo weak interactions. A fermion is left-handed (right-handed) if the direction of its spin is in the opposite (same) direction of its motion.

The three hadrons treated in this thesis are Λ, $\bar{\Lambda}$ and K_s^0, and they all decay via weak interactions. In Figure 2.4.1(a), a K_s^0 meson decays weakly to a positive and negative pion. When decaying, the $\bar{s}$-quark ($T_3 = +\frac{1}{2}$) emits a virtual W^+ boson and by doing so transforms into an $\bar{u}$-quark ($T_3 = -\frac{1}{2}$). In a similar way, the s-quark transforms into an u-quark by emitting a virtual W^- boson in Figure 2.4.1(b), which demonstrate the Λ decaying to a proton and a negative pion.

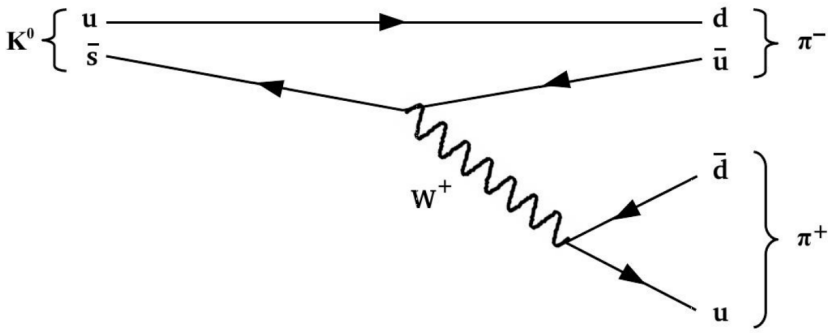

(a) The dominant decay channel of the K_s^0 meson.

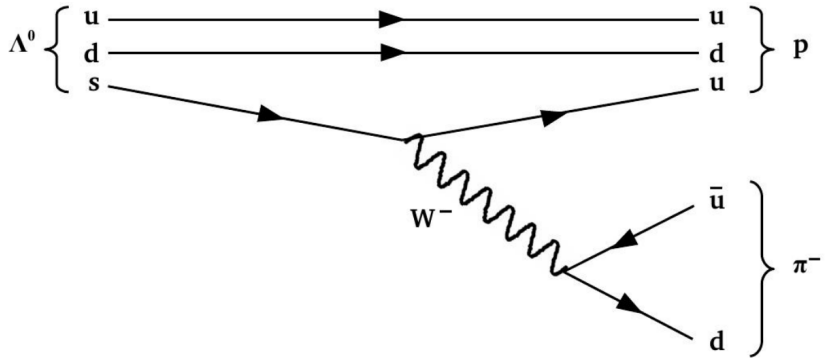

(b) The dominant decay channel of the Λ^0 baryon.

Figure 2.4.1: In the Feynman diagram (a), the K_s^0 meson decays to a positive and a negative pion, and in (b), the Λ^0 baryon decays to a proton and a negative pion. The Feynman diagrams are taken from [14].

3 High-Energy Physics

In this chapter, some concepts and variables associated with ultra-relativistic particle[6] collisions will be presented, with the focus on heavy-ion (A-A) and proton-proton (pp) collision. In a heavy-ion collision, two nuclei consisting of a large number of nucleons, such as lead (Pb) or gold (Au), are colliding. These types of collisions usually produce a large system of particles. Whereas, smaller systems of particles are produced by either colliding two protons or a proton and a nucleus (p-A).

[6] A particle is ultra-relativistic when it is moving at a speed very close to the speed of light c.

3.1 Collision Variables

Measurable observables are needed in order to test validity of the theories. The transition from mathematical theories to experimental particle physics is accomplished by the phenomenology part in particle physics. Relevant concepts and kinematic variables that relate the detected particles to the dynamics of high-energy collisions are explained and defined here. All numbered equations are expressed in natural units with $c = 1$. For a more thorough explanation of the variables, see Reference [8, 12, 13].

3.1.1 Invariant Mass

In high-energy particle collisions, new unstable particles can be created and some of these will decay before reaching the detectors. The final-state particles long-lived enough to reach the detector can be used to deduce which unstable particles were produced in the collision.

The energy $E = \gamma mc^2$ and momentum[7] $\mathbf{p} = \gamma m\mathbf{v}$ of a particle form the four-vector $p^\mu = (E, p_x, p_y, p_z)$, which is referred to as the four-momentum of the particle. The scalar product of the particle's four-momentum is a Lorentz invariant quantity[8] $p^\mu p_\mu = E^2 - \mathbf{p}^2$, and for a particle with mass m at rest $p^\mu = (m, 0, 0, 0)$, the scalar product is

$$p^\mu p_\mu = m^2 = E^2 - \mathbf{p}^2 \tag{3.1.1}$$

This is the Einstein energy-momentum relation and it holds in all inertial frames. When a particle decays, energy and momentum will be conserved and thus, also its four-momentum. Therefore, the kinematics for n decay products can be written as

$$p^\mu p_\mu = \left(\sum_{i=1}^{n} E_i\right)^2 - \left(\sum_{i=1}^{n} \mathbf{p}_i\right)^2 \tag{3.1.2}$$

and this gives the squared rest mass of the mother particle, i.e. its *invariant mass*.

The invariant mass of a mother particle can be calculated by measuring the momentum $\mathbf{p}$ and energy E of the decay products. By the above equation, a two-body decay of a particle a, where the decay products have four-momenta p_b and p_c, can be expressed as

$$m_a^2 = (p_b + p_c)^2 = (E_b + E_c)^2 - (\mathbf{p}_b + \mathbf{p}_c)^2 = m_b^2 + m_c^2 + 2(E_b E_c - \mathbf{p}_b \cdot \mathbf{p}_c) \tag{3.1.3}$$

where the square root of m_a^2 gives the invariant mass of the mother particle a.

3.1.2 Center-of-Mass Energy

The center-of-mass energy $\sqrt{s}$ is the energy available to produce new particles in collisions. It is a Lorentz invariant quantity derived from the energy-momentum relation.

[7] The Lorentz factor γ is defined as $\gamma = \frac{1}{(\sqrt{1-v^2/c^2})}$, where c is the speed of light in vacuum and v the velocity.

[8] A quantity is (relativistic) Lorentz invariant if it is invariant under a transformation between two coordinate frames that are moving at constant velocity relative to each other.

The $\sqrt{s}$ is given by the total energy E and three-momentum $\mathbf{p}$ of two initial-state particles, which can be expressed as the Equation 3.1.2. For a fixed target experiment, which takes place with one particle at rest in the laboratory frame, the conservation of momentum implies that the final-state particles must be in motion. This means that significant amount of the initial beam energy will reappear as kinetic energy of the final-state particles and will therefore not be available for particle production.

In colliding-beam experiments, much higher center-of-mass energies are achieved since the collision occurs in the center-of-mass frame. Consider a pp collision where the colliding protons have the same mass and energy, i.e. the four-momenta $p_1 = (E, \mathbf{p})$ and $p_2 = (E, -\mathbf{p})$. Inserting p_1 and p_2 in Equation 3.1.2 gives

$$p^\mu p_\mu = (p_1 + p_2)^2 = (E + E)^2 - (\mid \mathbf{p} \mid + (- \mid \mathbf{p} \mid))^2 = 4E^2 \tag{3.1.4}$$

where the square root of the above equation is the center-of-mass energy $\sqrt{s} = 2E$. The pp collisions analyzed in this thesis had a beam energy of $E = 6.5$ TeV, yielding a $\sqrt{s} = 13$ TeV.

3.1.3 Three-Momentum, Rapidity and Pseudorapidity

A particle produced in a relativistic collision is characterized by its four-momentum $p^\mu = (E, \mathbf{p})$, where the three-dimensional momentum vector $\mathbf{p} = \gamma m \mathbf{v} = (p_x, p_y, p_z)$. Most detectors in modern collider experiments are cylindrical where the beam axis defines the z-axis, and the azimuthal angle φ and the polar angle θ are in the xy-plane and the xz-plane, respectively. When operating at relativistic energies, it is not always trivial to measure the four-momenta of the produced particles and thus, some new variables need to be introduced.

The center-of-mass frame of the relativistic particles brought together to collide will move at some velocity along the z-axis and this generates a boost in z-direction of the detected particles. In order to study the particles in the center-of-mass frame, the quantity *rapidity* is introduced. The dimensionless rapidity y is additive under a Lorentz boost and defined as

$$y = \frac{1}{2} \ln \left(\frac{E + p_L}{E - p_L} \right) \tag{3.1.5}$$

where E is the total energy of the particle and p_L its longitudinal momentum along the beam axis ($p_L = p_z$). The rapidity is a relativistic implementation of a particle's velocity, which is not Lorentz invariant, and it takes values between $-\infty < y < \infty$, where infinity corresponds to the rapidity of c. When a relativistic particle is moving in the positive z-direction, $E \simeq p_z$ and $y \to +\infty$. Similarly, moving in the negative z-direction gives $y \to -\infty$. This means that the maximum scattering (90° angle w.r.t the beam axis) of a particle in a collision leads to a rapidity close to zero. Hence, the rapidity relates the angle between the xy-plane and the direction of an emitted particle produced in the collision. The two regions $y > 0$ and $y < 0$ are referred to as the forward and backward region, respectively.

Measuring the rapidity of a relativistic particle can sometimes be troublesome since both its energy and momentum are required. The energy can sometimes be measured directly by detectors and if that is not possible, it can be calculated by the energy-momentum relation. However, the calculation requires that the three-momentum can

be measured. At high rapidity values, the p_z becomes large and difficult to measure. To get around this problem, the pseudorapidity can be used instead. The pseudorapidity η depends solely on the angle θ and it is defined as

$$\eta \equiv -\ln(\tan(\theta/2)) \tag{3.1.6}$$

The polar angle takes the values $0^\circ < \theta < 180^\circ$. This means that $\eta \to \infty$ for $\theta = 0^\circ$, which is along the positive beam direction, and $\eta \to -\infty$ for $\theta = 180^\circ$, which is along the negative beam direction. If a particle is scattered 90° in the collision, that is completely perpendicular to the beam direction, then $\eta = 0$.

The pseudorapidity is not additive under a Lorentz boost. However, at truly relativistic energies, the rest masses of the particles can be neglected since $m << |\mathbf{p}|$. Thus, the total energy of a particle is approximately its three-momentum $E \approx |\mathbf{p}|$. By expressing the pseudorapidity as a function of

$$\eta = \frac{1}{2}\ln\left(\frac{|\mathbf{p}| + p_L}{|\mathbf{p}| - p_L}\right) \tag{3.1.7}$$

it is clear that the pseudorapidity converges to the definition of rapidity, $y \approx \eta$, at high energies.

Finally, a commonly used momentum variable in particle physics is the transverse momentum p_T. It is the magnitude of the two-momentum vector in the xy-plane perpendicular to the beam axis. The p_T is invariant under a Lorentz boost along the beam axis and is be defined as

$$p_\mathrm{T} = \sqrt{p_x^2 + p_y^2} \tag{3.1.8}$$

The p_T-spectra of identified particles produced in the collisions are important analysis tools. When studying the properties of the QGP, the p_T-spectra reflect the evolution of the particle system and which QCD processes involved.

By choosing the variables p_T, η, φ, y or η, the properties of the particles remain unchanged when going from the centre-of-mass frame to the laboratory frame. If needed, the cartesian momenta (p_x, p_y, p_z) of the particles can be obtained by the following conversions

$$\begin{aligned} p_x &= p_\mathrm{T}\cos\varphi \\ p_y &= p_\mathrm{T}\sin\varphi \\ p_z &= \sqrt{|\mathbf{p}|^2 - p_\mathrm{T}^2} \end{aligned} \tag{3.1.9}$$

3.1.4 Collision Centrality and Multiplicity

A key observable when characterizing the properties of a collision is *charged-particle multiplicity* (from hereon referred to as multiplicity). The geometry of a collision cannot be measured directly. Instead, experimental observables that have a direct correlation to the collision geometry are used when classifying the events according to their collision *centrality*. The multiplicity is such an observable and it measures the charged particle production in high-energy collisions.

In heavy-ion collisions, the centrality depends on the impact parameter b, which is defined as the distance between the centers of the two colliding nuclei. Since the impact parameter cannot be measured directly, the multiplicity can be used instead when determining the centrality of the collision. Before the collision point, the nuclei will be Lorentz contracted in their direction of motion and thus, appear as two thin discs in the center-of-mass frame. When colliding, the two nuclei will have an overlap region where there is a possibility for the nucleons to interact. The interacting nucleons, which undergo at least one inelastic scattering, are referred to as *participants*, while the nucleons that did not interact are referred to as *spectators*. In central collisions, when $b \to 0$, the large overlap region gives rise to a large volume of interacting nucleons that produces a high multiplicity. Similarly, in a peripheral collision, when b is large, the volume of interacting nucleons will be small, yielding a low multiplicity.

When colliding two protons, inelastically scattered partons can be thought of as the participants. In a similar way as for heavy-ion collisions, the multiplicity can be used when estimating the number of interacting partons in pp collisions. If the quarks and gluons of the colliding protons interact by inelastic scattering, new particles will be produced. In central or head-on collisions, numerous partons will interact, resulting in high multiplicities. While for more peripheral collisions, fewer partons will interact resulting in low multiplicities. However, the initial-state geometry is not given for a pp collision and instead, the collisions are solely characterized by the final-state particles, i.e. the multiplicities. In this thesis, the multiplicity measurement was performed by the VZERO detector in ALICE, and it will be further discussed in Section 4.1.3.

3.2 Quark Gluon Plasma in Heavy-Ion Collisions

The system produced in a relativistic heavy-ion collision undergoes different stages, which can be divided into the pre-equilibrium (QGP formation), expansion, hadronization, and freeze-out stage. In the pre-equilibrium stage a fireball is produced by the initial partonic collision. The highly excited fireball will rapidly establish local thermal equilibrium through the constituents of the system colliding at a high frequency. However, it is unclear how equilibrium can be achieved so quickly and the first stage where the QGP formation occurs is the least understood [12].

After the system established equilibrium, it will undergo collective expansion due to the gradient force acting upon it. The QGP phase have been observed to behave almost as an ideal fluid[15] and when an ideal fluid expands, almost no entropy is generated, making the expansion reversible. Hence, the expansion of the QGP is spatially reversible. The expansion stage will generate an important QGP characteristics known as collective flow. As the system expands, the energy density decreases and hence the temperature also decreases. Eventually, the temperature of the system goes below $\sim T_c$, and the parton matter in the QGP starts to form hadronic matter and thus, the system enters the hadronization stage. The hadronization stage of the QGP is a non-perturbative process and is also not fully understood.

The last stage, the freeze-out, is a sequence of two steps, chemical and kinetic freeze-out. In the chemical freeze-out, local equilibrium is still maintained by hadrons colliding frequently . The rate of the inelastic collisions, which makes it possible for

the hadrons to change their identities, becomes low compared to the expansion rate and therefore, the hadron abundances are fixed after this stage. The kinetic freeze-out occurs when the average distance between the hadrons is larger than the range of the strong interaction and the collision frequency is not high enough to maintain local equilibrium. After the kinetic freeze-out, the momentum of the hadrons are fixed as they propagate to the detectors[12].

3.2.1 Observables of the QGP

To establish whether the QGP phase is created or not in ultra-relativistic heavy-ion collision, it is important to know which experimental observables indicate QGP formation. The QGP created in a collision is a transient state that cannot be observed directly. This means that all information about the QGP must be extracted from the detected final-state particles. Assuming that the hadronization does not fully erase the memory of the constituents in the QGP, the final-state hadrons can be used as a probe when studying the QGP since their properties reflect the stages before the hadronization [12]. Both electromagnetic and hadronic probes are used when studying the QGP. However, electromagnetic probes will not be elaborated on since only hadronic probes are of relevance for the analysis in this thesis.

The hadronic probes can to some extent be categorized as *hard* or *soft*, depending on the QCD processes involved. Hard probes are generated by interactions with high-momentum transfers. For example, jets emerge from hard QCD interactions and will be quenched if they have to propagate through a dense strongly interacting medium. Soft probes emerge from interactions involving low-momentum transfer and are measured by parameters describing the collective behavior of the medium. Four different QGP observables will be briefly explained below.

Collective Flow

Collective flow is a phenomenon generated by the early stage of the QGP phase evolution. If the system established equilibrium after the collision, it will undergo a collective expansion before hadronization. The system will be surrounded by vacuum and this, together with the dense nature of the system, will give rise to a pressure gradient from the center of the system to its boundary. The collective expansion generates radial flow and anisotropic flow. The anisotropic flow is characterized by the flow harmonics v_n, which are determined by measuring the azimuthal (φ) distribution of the final-state hadrons with respect to the reaction plane. The reaction plane is spanned by the beam direction and the impact parameter. The azimuthal particle distribution can be expressed with a Fourier expansion, where the Fourier coefficients correspond to the flow harmonics [16].

In a central heavy-ion collision, the radially symmetric pressure gradient will boost the hadrons with a radial velocity $\mathbf{v}$. This means that the heavier hadrons will gain more momentum ($\mathbf{p} = \gamma m \mathbf{v}$) giving rise to a mass hierarchy in the p_{T}-spectra. The abundance of low-p_{T} hadrons will shift to higher p_{T} by the radial flow and this effect will be more pronounced for the heavier hadrons.

The anisotropic flow parametrized by the harmonics v_n in the Fourier expansion, where each harmonic corresponds to a different type of anisotropy. The dominant contribution for the anisotropic flow is the *elliptic flow*, which is given by the second Fourier coefficient v_2 [17]. The elliptic flow is dependent on the impact region in heavy-ion collisions, where less central collisions, which give rise to an almond shape geometry of the system, produce the highest v_2 values. The elliptical shape of impact volume leads to a pressure gradient in the reaction plane along b that generates an anisotropic momentum distribution. The first analysis of elliptic flow performed by RHIC supported the prediction of the QGP phase approaching a perfect liquid[13].

Strangeness Enhancement

Hadrons that are composed of one strange quark (or several strange quarks) are referred to as strange hadrons (or multi-strange hadrons). An abundance of strange hadrons in heavy-ion collisions was one of the first QGP signatures to be proposed [18]. Originally, the idea of strangeness enhancement was to compare the production of strange particles in A-A collisions, normalized to the multiplicity, to the corresponding quantities in pp (or p-A) collisions. Experimental results do indeed demonstrate such enhanced production of strange hadrons in A-A collisions compared to pp and p-A collisions [19]. Even so, strangeness enhancement is still of interest when searching for QGP signatures in small systems and such analysis can be performed by studying the multiplicity dependence of the strangeness production in pp and p-A collisions.

Out of the three light quark flavors (u, d, s), the strange quark is the heaviest and unlike the two lightest quarks, the strange quark is not present in the initial state of the collision. Hence, the identified strange hadrons are the result of the strange quarks produced in the collision. In the early stage of the collisions, hard partonic scattering processes produce $s\bar{s}$-pairs by the fusion of two gluons or two light quarks ($gg \leftrightarrow s\bar{s}$ and $q\bar{q} \leftrightarrow s\bar{s}$), where gluon fusion is the dominant production channel [20]. The momentum exchange needed for these processes, $Q \sim 2m_s$, is lower when the quarks and gluons are deconfined. In the deconfined state, it is the bare mass of the strange quark $m_s \sim 0.1$ GeV that determines the minimum momentum exchange Q needed for the process to occur. While in a hadron gas where the quarks and gluons are confined, it is the constituent mass of the strange quark, which is approximately 0.5 GeV, that sets the threshold energy Q [18]. If the QGP phase was created in the collision, an abundance of strange quarks is expected compared to a collision with no QGP phase. In the hadronization stage, the non-strange quarks will combine with the numerous strange quarks leading to enhanced strange hadron yields.

Jet Quenching

To understand why jet quenching is a signature of the QGP phase, it is important to first understand the origin of jets. The separation of an energetic quark-antiquark ($q\bar{q}$) pair created in a collision, will generate a strong interaction process called fragmentation. To conserve momentum, the $q\bar{q}$ pair will be scattered back-to-back in the center-of-mass frame. When being separated, the $q\bar{q}$ pair converts its energy into collimated showers of hadrons. As explained in Section 2.3.2, a strong color field is created

when two quarks are separated. To reduce the energy in the field, the partons will radiate gluons that fragment into hadrons along the way or break up the color field by forming a $q\bar{q}$ pair [12]. The processes of creating $q\bar{q}$ pairs and radiating gluons will go on until the original energy is dissipated. The detected shower of hadrons will have high p_{T}-values and their directions will reflect the direction of the quark or antiquark that were scattered in the collision.

If the QGP medium is created in the collision, scattered high-energy partons will have to traverse the strongly coupled medium before fragmenting into hadrons. The partons will interact with the medium and thus, lose a significant amount of their momenta. This energy loss leads to a high-p_{T} suppression of the particle yield. Hence, in a heavy-ion (A-A) collision with the QGP phase present, the number of particles with high p_{T} is expected to be less than in a pp collision [12]. To the left in Figure 3.2.1, a dijet event[9] in a pp collision is shown. Since the partons can propagate freely, two distinct jets of high-p_{T} hadrons are produced in the final state. The right picture in Figure 3.2.1 shows a dijet event in a A-A collision where the QGP phase is created. Two energetic quarks are scattered near the surface of the medium, one of the quarks will escape the medium and fragments into a hadron jet, while the other quark enters the medium. The quark that passes through the medium will lose a large fraction of its energy by interacting with the medium. When the quark exits the medium and fragments, the detected hadrons will have significantly lower p_{T}-values than the fragments of the quark that did not pass through the medium. Result from Au-Au collisions at RHIC in 2003 showed that mesons were highly suppressed at high p_{T}, while photons were not. Thus, the high-p_{T} suppression must originate from a final state effect. The photons do not carry color charge and therefore can traverse a highly dense colored medium unaffected, while highly energetic color charged particles that give rise to final-state hadrons (like mesons) will be quenched by parton-medium interactions. This observation provided strong evidence for the QGP phase being created in heavy-ion collisions.

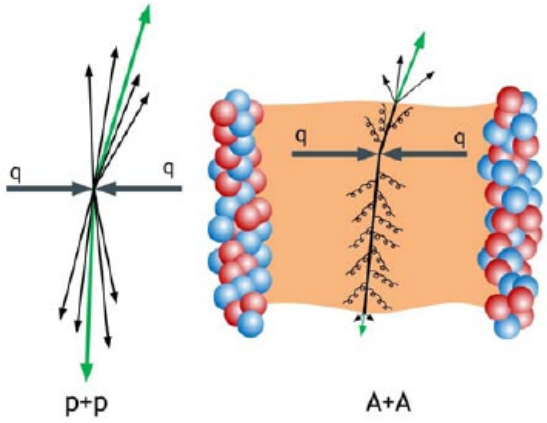

Figure 3.2.1: The figure illustrates hard scattering of two quarks in a proton-proton collision (left) and in an nucelus-nucelus collision (right). In the proton-proton collision, the two scattered quarks fragment into two jets of high-p_{T} hadrons. In the nucleus-nucles collision, one of the jets enters the strongly coupled medium and loses energy due to parton-medium interactions. The figure is taken from [21]

Baryon-to-Meson Ratio

Enhanced baryon-to-meson ratio in the intermediate range $2 < p_{\mathrm{T}} < 5$ GeV/c for heavy-ion collisions compared to pp collisions was first observed by experiments at

[9] A dijet event is a particle collision where two jets were produced.

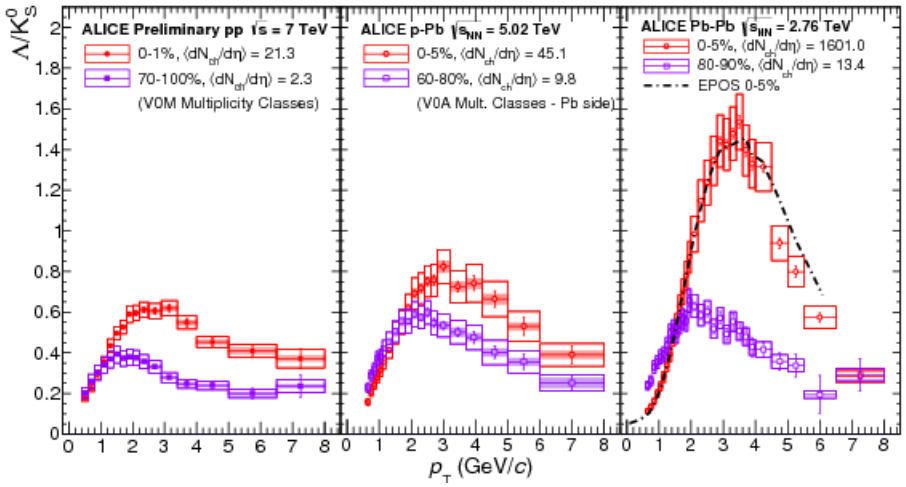

Figure 3.2.2: The Λ/K^0_s ratio for central and peripheral pp, p-Pb, and Pb-Pb collisions [27].

RHIC [22, 23], and similar enhancement has been observed by ALICE at the LHC [24, 25]. In this p_T-range, parton fragmentation is assumed to dominate the particle production. The observed enhancement can be interpreted with a hydrodynamic description [26]. The QGP phase is created in local thermal equilibrium and when it expands, it will assign a common radial velocity independent to the final-state particles, where the heavier particles will gain more momenta giving rise to the enhanced baryon-to-meson ratio, which is demonstrated in Figure 3.2.2. The figure shows the Λ/K^0_s ratio for pp, p-Pb, and Pb-Pb collisions, where the enhancement is most pronounced for central Pb-Pb collisions where the QGP volume is largest.

3.3 QGP Features in Small Systems

The small systems produced in ultra-relativistic p-A and pp collisions have historically formed the reference baseline when studying the QGP properties in heavy-ion collisions. By comparing the behavior of the large systems to the small systems, it has been possible to establish strong proof for a phase transition from hadronic matter to a plasma of deconfined quarks and gluons in heavy-ion collisions [3]. Whether something similar to the QGP phase is created or not in small systems is still not established. However, there are indications that the high multiplicity systems produced in pp and p-Pb collisions exhibit similar behavior to those created in heavy-ion collisions. Results of high multiplicity events in pp and p-Pb collisions from experiments at the LHC show that there is flow-like behavior in small systems [4, 5, 6]. Furthermore, strangeness enhancement in high multiplicity pp collisions has been observed by ALICE at the LHC [28]. But whether such effects originate from a formation of a strongly coupled medium similar to QGP or from initial state effects is not yet clear.

The result in Figure 3.3.1 is published by ALICE [29], and it shows the average transverse momentum $< p_T >$ as a function of the event multiplicity N_{ch} for pp, p-Pb and Pb-Pb collisions. The pp collisions exhibit a rapid increase of $< p_T >$ with increasing N_{ch} and the high multiplicity events are generated by hard QCD processes,

such as jet production. For Pb-Pb, the increasing curve of the $< p_{\mathrm{T}} >$ is eventually saturated, despite increasing multiplicity. Collective soft QCD processes and hard QCD processes, such as jets, generate high multiplicities. However, the hard QCD processes will be heavily suppressed in the Pb-Pb collisions resulting in dominating low $< p_{\mathrm{T}} >$.

When studying the properties of the QGP phase, most of the observables contain contributions from both soft and hard QCD processes [30]. It can therefore be difficult to observe QGP-like features in pp collisions since the competing soft and hard QCD processes may not generate the same outcomes as those observed in heavy-ion collisions. For example, due to the small size of the system in pp collisions, jets cannot be quenched to the same extent as in Pb-Pb collisions and this will give rise to harder p_{T}-spectra of the identified hadrons in pp collisions.

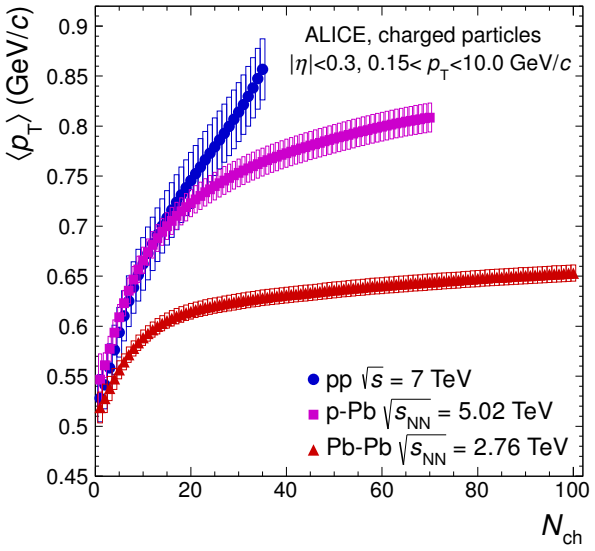

Figure 3.3.1: The average transverse momentum $< p_{\mathrm{T}} >$ versus charged-particle multiplicity N_{ch} in pp, p-Pb, and Pb-Pb collisions. Figure taken from [29]

By performing an event shape analysis, we try to isolate the collisions where jets (hard processes) dominate from those where low-momentum partonic scattering dominate (soft processes). Thus, the effects of the soft and hard processes on the hadron productions in the pp collisions can be analyzed (to some extent) separately. The *transverse spherocity* is a variable with such purpose of characterizing the events and it will be discussed in the next section.

3.4 Transverse Spherocity

The event shape variable used in this thesis is the transverse spherocity S_O. For each collision, the S_O measures the geometrical distribution of the transverse momenta (p_{T}) of the produced charged hadrons [30]. The restriction to the transverse plane makes the S_O invariant under a Lorentz boost along the beam axis. The S_O is defined as

$$S_O = \frac{\pi^2}{4}\left(\frac{\sum_i \mid \mathbf{p}_{\mathrm{T}i} \times \hat{\mathbf{n}} \mid}{\sum_i p_{\mathrm{T}i}}\right)^2 \tag{3.4.1}$$

The sums extend over each $p_{\mathrm{T}i}$ (the magnitude and the vector) of all charged tracks in the collision. The transverse unit vector $\hat{\mathbf{n}}$ minimizes the ratio. The S_O takes on values between the two limits 0 and 1, and these limits are related to specific geometrical arrangements in the transverse plane

$$S_O = \begin{cases} 0 & \text{"jetty" limit (hard QCD)} \\ 1 & \text{"isotropic" limit (soft QCD)} \end{cases} \tag{3.4.2}$$

When $S_0 \to 0$, the charged hadrons produced in the collision will be unevenly distributed, giving rise to a "pencil-like" geometrical shape. This shape indicates that jets were produced in the collision which is an effect of hard QCD processes. The limit when $S_0 \to 1$ corresponds to a collision where the outgoing charged hadrons are evenly distributed, which would be an effect of the soft QCD processes.

4 The ALICE Experiment

The Large Hadron Collider (LHC) is a part of the accelerator complex at the European Organization for Nuclear Research (CERN), which is based in a suburb of Geneva in Switzerland. At the LHC, beams of protons or heavy nuclei are accelerated to high energies before colliding. The beams are traveling in opposite directions in two separate synchrotron rings, which are kept at ultrahigh vacuum ($10^{-10} - 10^{-11}$ mbar). The rings are located ∼100 m underground and they both have a circumference of 26.7 km [31]. Strong electromagnetic fields, provided by superconducting electromagnets, are used for both accelerating the beams and to direct them around the accelerator. Dipole magnets bend the beams, while quadrupole magnets keep the beams focused. The high energies of the beams are achieved by 16 radiofrequency (RF) cavities along the rings. Electromagnetic fields of 5 MV/m accelerate charged particles when they pass through the cavities. The fields in the RF cavities are made to oscillate and the oscillation splits the beams into bunches of particles.

By the design of the LHC, the maximum center-of-mass energy is $\sqrt{s} = 14$ TeV for proton-proton (pp) collisions, and $\sqrt{s_{NN}}$[10] $= 5.5$ TeV for lead-lead (Pb-Pb) collisions [31]. In *Run 1* (2009-2013), the LHC reached collision energies of $\sqrt{s} = 8$ TeV for pp, $\sqrt{s_{pN}} = 5.02$ TeV for p-Pb, and $\sqrt{s_{NN}} = 2.76$ TeV for Pb-Pb. In March 2015 the LHC *Run 2* started after a two year technical stop during which the magnets were upgraded in order to achieve higher beam energies. In Run 2 (2015-2018), collision energies of $\sqrt{s} = 13$ TeV for pp collisions and $\sqrt{s_{NN}} = 5$ TeV for Pb-Pb collisions have been achieved.

There are four intersection points at the LHC where the beams collide. The ALICE (A Large Ion Collider Experiment) detector is located at one of these points (referred to as P2) and is one of the four main experiments operating at the LHC. ALICE is the only dedicated heavy-ion experiment at the LHC and its main focus of research is strongly interacting matter. Therefore, the design of the ALICE detector is optimized to cope with the highest event multiplicities anticipated at the LHC [32].

4.1 The Detector Systems

The ∼10,000 tonne ALICE detector, with its overall dimensions $16 \times 16 \times 26$ m^3, is located 56 m underground and consists of in total 17 detector systems [33]. The detector systems, which are shown in Figure 4.1.1, can be divided into three categories: central barrel detectors, forward detectors, and the MUON spectrometer. The ALICE coordinate system is a right-handed orthogonal Cartesian system, where the origin $(x, y, z) = (0, 0, 0)$ is at the detector center (the nominal interaction point of the

[10]The notation NN refers to the available center-of-mass energy per nucleon pair.

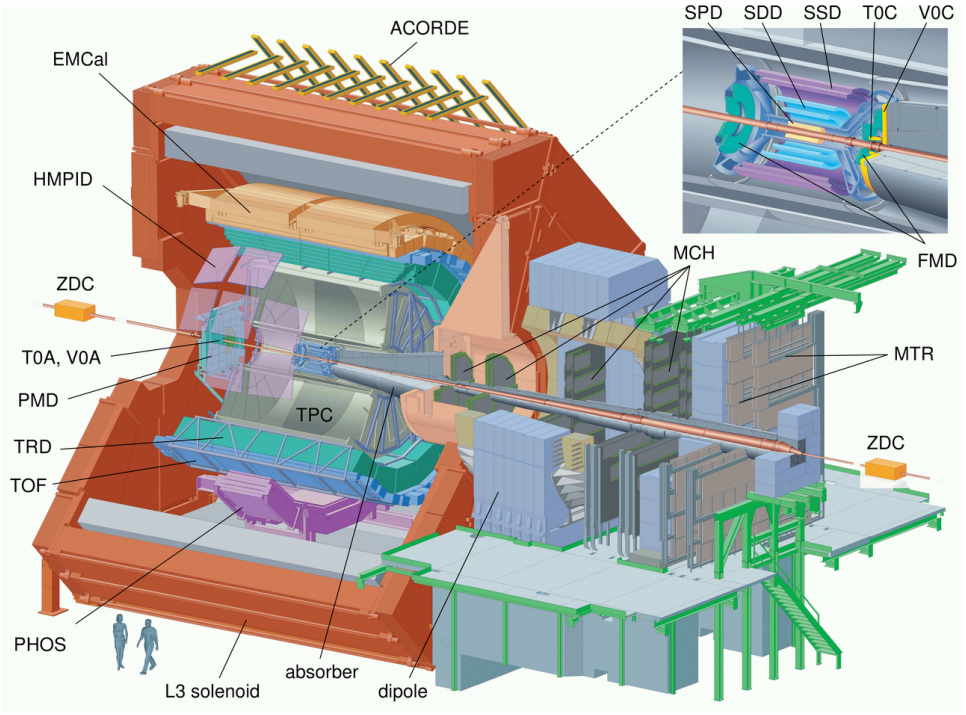

Figure 4.1.1: The ALICE subdetectors. The central-barrel detectors: ITS (composed of the detector systems SPD, SDD, and SSD), TPC, TRD, TOF, PHOS, EMCal, and HMPID. The forward detectors: PMD, FMD, VZERO (V0A and V0C) , T0, and ZDC. The Muon Trigger, MTR, and the Muon Chambers, MCH, are the two detector systems of the MUON spectrometer. ACORDE is located on top of the magnet. The schematic illustration is taken from [33].

beams). The x-axis is horizontal and perpendicular to the beam direction, which defines the z-axis. The positive direction of x is towards the center of the LHC. The y-axis is vertically perpendicular to the beam direction and its positive direction is upwards. The z-axis is positive, from the point of the origin, along the direction away from the MUON spectrometer.

The central-barrel detectors include the Time Projection Chamber (TPC), Inner Tracking System (ITS), Transition Radiation Detector (TRD), Time Of Flight (TOF), Photon Spectrometer (PHOS), Electromagnetic Calorimeter (EMCal), and High Momentum Particle Identification Detector (HMPID). The TPC, ITS, TRD, and TOF cover the entire azimuthal angle at mid-pseudorapidity $|\eta| \lesssim 0.9$ [33]. All of the central-barrel detectors are symmetric around $\eta = 0$ and embedded in the L3 solenoid magnet with a magnetic field, $B = 0.5$ T, parallel to the beam axis. The TPC and ITS are the main tracking detectors. They reconstruct the trajectories of the charged particles in space and measure their momentum. The EMCal and PHOS measure the total energy of electrons and photons as they interact with multiple layers of matter resulting in the particles energies being absorbed. EMCal has a significantly larger acceptance than PHOS, while PHOS has a significantly better energy resolution than EMCal. The HMPID identify high-p_{T} particles and the TRD focuses on the identification of electrons. The TOF determines the flight time of the particles, i.e. from the interaction

point to the detector's location. The ITS and the TPC were used for the analysis in this thesis and will be elaborated on in the following sections.

The ALICE forward detectors are the Photon Multiplicity Detector (PMD), silicon Forward Multiplicity Detector (FMD), Zero Degree Calorimeter (ZDC), the quartz Cherenkov detector T0, and the plastic scintillator detector VZERO. The forward detectors cover the parts where $|\eta|$ is large, meaning that they are positioned at small angles with respect to the beam axis. The PMD and the FMD measure photons and charged particles, respectively. The T0 detector measures the start time, which is used by TOF to determine the flight time, and the longitudinal position of the interaction point. The VZERO and ZDC are used for determination of the collision centrality. The VZERO detector was used for the multiplicity determination in this thesis and will be discussed below.

The MUON spectrometer consists of two detector systems, the Muon Chambers (MCH) and the Muon Trigger (MTR), and its purpose is to reconstruct heavy flavors through the $\mu^+\mu^-$ decay channel. The MCH measure the light vector meson and quarkonium[11] productions in the backward rapidity region and the MTR provides single-muon and muon-pair triggers. The ACORDE (A Cosmic Ray Detector) is a cosmic-ray trigger detector used for calibration purposes.

4.1.1 The Time Projection Chamber

The Time Projection Chamber (TPC) covers the full azimuthal angle and the mid-pseudorapidity region of $|\eta| < 0.9$. The TPC is used to reconstruct and identify particles produced in the collisions by measuring their ionization trajectories and ionization energy losses.

The detector is a hollow cylinder consisting of a 88 m^3 drift volume filled with a Ne-CO_2 gas mixture. It is located in the central-barrel of ALICE, where it is enclosed by the TRD and surrounds the ITS. The cylinder is aligned with the beam axis and also parallel to the central-barrel's magnetic field of 0.5 T. The device has an inner radius of 85 cm, an outer radius of 250 cm and a total length of 500 cm [34]. At the ends of the cylinder, Multi-Wire Proportional Chambers (MWPCs) are located. A conducting electrode, charged at -100 kV, is situated at the axial center of the TPC and divides the cylinder into two drift regions. The gas in the chamber, which is at atmospheric pressure, is ionized when charged particles traverse the detector. The liberated electrons drift towards the end plates due to the electric field present in the detector. The arrival times of the electrons are detected when they reach the MWPCs. By comparing the arrival time to the collision start time, the drift time of the electrons can be measured. The MWPCs determine the x and y components of the trajectories of the charged particles in three-dimensional space, whereas the drift time and drift velocity reconstruct the z component with high accuracy. Furthermore, the particle ionization trajectory will have a momentum dependent curvature due to the magnetic field. The curvature is used for determining the momentum of the charged particle.

In addition to the determination of spatial coordinates and momentum, the TPC provides particle identification (PID). The PID is performed by measuring the parti-

[11] Quarkonium usually refers to heavy quark mesons such as charmonium and bottomonium, which consist of $c\bar{c}$ and $b\bar{b}$, respectively.

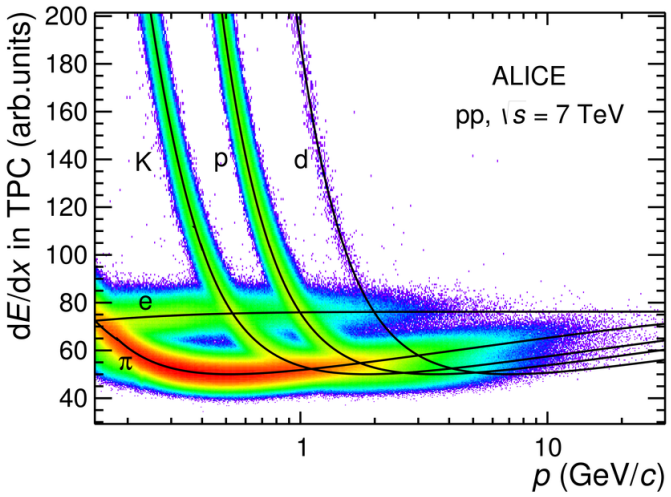

Figure 4.1.2: The particle energy loss per distance unit $\mathrm{d}E/\mathrm{d}x$ as a function of the momentum measured by the TPC. The plot shows distinct bands of electrons, pions, kaons, protons, and deuterons. Figure taken from [35].

cle's energy loss by ionization of atoms when traveling a distance x in the detector, $-\mathrm{d}E/\mathrm{d}x$. The energy loss of a particle with charge z (in units of e) in matter can be described by the Bethe-Bloch equation, which takes (approximately) the form [11]

$$-\frac{dE}{dx} = Kz^2\frac{Z}{A}\frac{1}{\beta^2}\left[\frac{1}{2}\ln\left(\frac{2m_ec^2\beta^2\gamma^2T_{max}}{I^2}\right) - \beta^2 - \frac{\delta(\beta\gamma)}{2}\right] \tag{4.1.1}$$

where $\beta = \frac{v}{c}$, $\gamma = (1-\beta)^{-1/2}$ (the Lorentz factor), I the mean excitation energy and $\delta(\beta\gamma)$ the density effect correction to the ionization energy loss. A and Z are the atomic mass and atomic number of the absorber. The constant $K = 4\pi N_A r_e^2 m_e c^2$, where N_A is Avogadro's number, and r_e and m_e the electron radius and mass. The maximum kinetic energy a charged particle, passing through the detector, can impart on a free electron is T_{max}. The kinetic energy of an incident particle is dependent on the particle's mass and velocity. Therefore, the $-\mathrm{d}E/\mathrm{d}x$ of the particles measured by the TPC as a function of the corresponding momentum p will generate distinct bands depending on the masses of the incoming particles. This can be seen in Figure 4.1.2, where the black lines demonstrates the PID of electrons (e), charged pions (π) and kaons (K), protons (p), and deuterons (d). These particle species can be produced directly and also feature prominently in the decay channels for many short-lived particles[12], which then can be identified by the invariant mass reconstruction (defined by Equation 3.1.3).

4.1.2 The Inner Tracking System

The Inner Tracking System (ITS) is located closest to the beam pipe. The main purpose of the ITS is to identify the weakly decaying heavy particles by determining, with high

[12]The particles that decay before reaching the detectors.

precision, the collision vertex and locating the secondary vertices. The ITS consists of six cylindrical layers of silicon detectors, two Silicon Pixel Detectors (SPDs), two Silicon Drift Detectors (SDD), and two Silicon Strip Detector (SSDs). The 2×3 layers make up the three detector systems in the ITS.

The general operation principle of a silicon semiconductor is to create a depletion region without movable charges by applying a reverse bias on the p-n junction. Electron-hole pairs will be created through ionization if charged particles are passing through the depletion region. The reverse bias field will then transport the electron-hole pairs to read out electronics creating signals proportional to the energy losses of the ionizing particles.

The SPDs are the two inner-most layers in the ITS. They cover the full azimuthal angle and counting from the beam pipe, have an acceptance of $|\eta| < 2.0$ and $|\eta| < 1.4$ [33]. They are composed by two-dimensional sensor modules, and each one of the modules consists of a silicon pixel matrix of 256×160 cells. The SPD system has an inner radius of 3.9 cm, and thus, the system is designed to manage the high track density that arises close to the collision point. Further, the SPD has a high spatial resolution that makes it ideal for reconstructing both the primary and secondary vertices.

The two intermediate layers in the ITS are the SDDs. The inner radius is 15 cm and both layers cover the full azimuthal angle and have an acceptance of $|\eta| < 0.9$. The SDD system has good spatial resolution and it is capable of determining the position of charged particles in two dimensions [36]. Furthermore, it provides energy loss measurements used for PID. The two SDD layers consist of large drift constructions and by measuring the drift time of electrons, which are created by ionizing particles in the depletion region, good tracking and PID performance of low-p_{T} particles can be achieved.

The outer-most layers consists of SSDs with the inner radius of 39 cm and both layers having an acceptance of $|\eta| < 1.0$ over the full azimuth. The two layers are composed by double-sided microstrip silicon sensors. The SSD system provides measurements of the track position in two dimensions and energy loss measurements.

Some of the main purposes of the ITS are to reconstruct tracks in the mid-rapidity region and to improve the angle and momentum resolution of the TPC. By matching the tracks in the ITS with the tracks reconstructed by the TPC, the PID performance of the TPC can be improved. The SDD and SSD provide PID in the low-momentum region (< 1 GeV) by the energy loss $\mathrm{d}E/\mathrm{d}x$ measurements. Further, by its high spatial resolution, the SPD serves as a primary and secondary vertex finder.

4.1.3 The VZERO Detector

The VZERO detector is one of the forward detectors of ALICE. The VZERO system provides minimum bias and centrality trigger for the experiment. Further, it measures the charged particle multiplicity in forward and backward pseudorapidity regions, the azimuthal distribution of the charged particles, and the beam luminosity. The measurement of the multiplicity is essential when estimating the collision centrality[37]. In this thesis, the event multiplicity was determined by the VZERO detector.

The system is composed by two scintillator detector arrays VZERO-A and VZERO-C, which cover the forward pseudorapidity region $2.8 < \eta < 5.1$ and backward pseu-

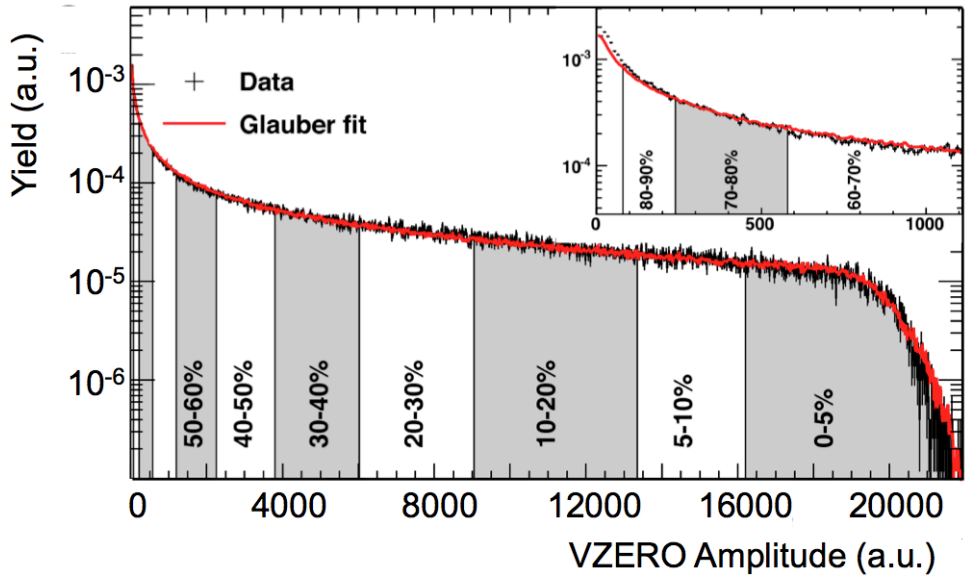

Figure 4.1.4: The black line shows the distribution of the sum of the amplitudes in the VZERO-A and VZERO-C in Pb-Pb collisions at $\sqrt{s_{NN}} = 2.76$ TeV [38]. The red line represents Glauber model fit. The centrality classes are shown in the distribution, where the low amplitude part of the distribution corresponds to the peripheral collisions (high percentage), while the high amplitude part corresponds to the central collisions (low percentage).

dorapidity region $-3.7 < \eta < -1.7$, respectively. Each detector is divided in four rings in the radial direction and in turn, each ring is divided into eight sections in the azimuthal direction. This gives the VZERO-A and VZERO-C in total 64 channels (32 channels each). The segmentation of VZERO-A and VZERO-C is shown in Figure 4.1.3. The detectors are made of plastic scintillators, with a thickness of 2.5 cm for the VZERO-A channels and 2.0 cm for the VZERO-C channels [37].

Charged particles entering the scintillators will lose energy by exciting and ionizing the atoms in the material. The excited and ionized atoms deposit the excess energy by emitting photons, where the number of photons is proportional to the energy loss of the charged particles. The emitted photons then enter photomultiplier tubes, where they will release electrons by hitting photocathodes. The released electrons are accelerated towards a series of electrodes, which have positive voltages, causing electron avalanches. Thus, the signal of an initial photon will be amplified before entering the VZERO front-end electronics where the signal is read out.

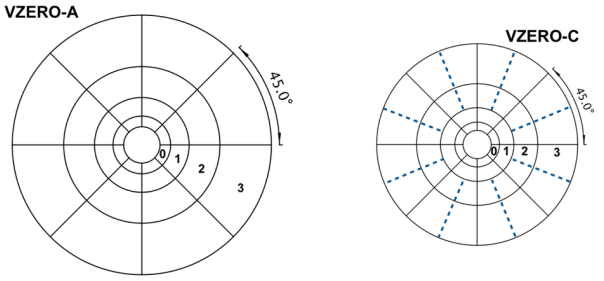

Figure 4.1.3: Sketches of the VZERO-A (left) and VZERO-C (right) segmentations. Figure taken from [37].

The multiplicity measurement provided by the VZERO is based on the energy

deposited in the scintillators. The sum of the signal amplitudes in the VZERO-A and VZERO-C for a number of events gives a distribution that is used for the centrality class or event multiplicity calculations. A typical VZERO amplitude distribution is shown in Figure 4.1.4, where low amplitudes correspond to peripheral collisions, while high amplitudes correspond to central collisions. The VZERO amplitude distribution is fitted with a Monte Carlo[13] Glauber model. For Pb-Pb collisions, the Glauber model describes the collision geometry in terms of the impact parameter, while pp collisions are classified solely by the event multiplicity. A low collision multiplicity will generate a low VZERO amplitude, whereas high multiplicity generates a high amplitude. The VZERO multiplicity is referred to as the V0M and it is expressed in percentages. For pp collisions, events in the V0M 0-5% class represents the 5% of the total set of analyzed collisions that produced the highest VZERO amplitude, that is the 5% events in the total data set with the highest multiplicities.

5 Analysis

This chapter presents the analysis method of reconstructing the strange hadrons K^0_s, Λ, and $\bar{\Lambda}$, and measure their respective p_T-spectrum. Further, the event shape analysis by transverse spherocity cuts for high multiplicity events is presented.

The reconstruction and signal extraction of the strange particles were evaluated using Monte Carlo (MC) simulated data before being applied on real data, where the MC and data sample included events from all multiplicity classes (V0M:0-100%). The uncorrected p_T-spectra of the strange hadrons for both the MC and data sample were compared before estimating the correction factors using the MC simulated data.

The particle reconstruction and signal extraction methods, along with the measured correction factors, were then directly applied on high multiplicity events (V0M:0-10%) and events selected by spherocity cuts. Only real data was used for the analysis performed on the high multiplicity and spherocity event selections.

5.1 Data Processing and Data Set

The results presented in this thesis were generated with the software AliROOT, which is the ALICE Offline framework for reconstruction, simulation and analysis [39]. The high-energy physics software ROOT is the foundation on which the AliROOT framework is directly built. ROOT was developed at CERN and it is an object-oriented C++ framework for data processing. The software is designed for storing and analyzing data of petabytes magnitude [40].

The data set used in this analysis contains pp collisions at $\sqrt{s} = 13$ TeV recorded by the ALICE detector in 2016 (Run 2) during the period LHC16l. In addition to the real data, MC simulated data was used. The MC data set is tuned to match the same conditions as for the real data set. In total, the real data set consists of 44.4×10^6 events and the MC data 42.2×10^6 events.

[13]Monte Carlo methods in particle physics are used for simulating particle collision systems and their many coupled degrees of freedom.

5.1.1 Monte Carlo Simulations

MC simulations are artificial data given by event generators. These generators produce, in accordance with theories and models, the systems of particles in the collisions. The pp collision events for the MC analysis were generated from PYTHIA [41]. To reproduce the process of detecting the particles (which is always the case in real collision data), each simulated particle propagates through the detector simulation package GEANT3. The GEANT3 program simulates the process of the particles passing through the ALICE detector. The MC data are then tuned according to the conditions of the real detectors at the time of data taking. Since the events are simulated, all the properties of every single particle produced in the collision are known. Each simulated particle is given a PDG (Particle Data Group) code[14] that holds all information about the particles.

The MC analysis included generated MC data (MC_{gen}) and reconstructed MC data (MC_{rec}). The generated MC data gives the particle distribution created at the collision point, *before* they enter the detectors. The reconstructed MC data gives the particle distribution *after* the particles have *passed through* the detector simulation and have been reconstructed in the same way as for real data. In this analysis, selection criteria were studied using MC_{rec} before applying them on the data set. In the MC analysis, the notation MC_{rec}^{PDG} means that PDG codes have been used to only select the K_s^0, Λ, and $\bar{\Lambda}$ particles that originate from the primary vertex and have the same decay channels as considered for real data. The notation MC_{rec}^{blind} means that no PDG codes were used when selecting the K_s^0, Λ, and $\bar{\Lambda}$ candidates and therefore, the MC_{rec}^{blind} represented the simulated yields treated as real data.

5.2 Event Selection

The basic event selection in this analysis was performed for all event multiplicities (V0M:0-100%) and required the events to pass the following selection criteria:

- The selected events were required to have at least one reconstructed SPD track within the pseudorapidity range of $|\eta| < 1.0$. By this requirement, only events with the number of inelastic scattered particles greater than zero (INEL>0) are selected.

- Only events with a reconstructed primary vertex at distance less than 10 cm from the nominal interaction point along the beam axis ($|z| < 10$ cm) were accepted. By this selection, the acceptance and efficiency biases for tracks at the edges of the TPC are reduced.

- Pile-up events, which contain multiple collisions, were removed by requiring SPD and tracking vertex consistency. For an event with two primary vertices, the vertex reconstructed by the SPD has to be within 0.5 cm in the z coordinate of the vertex reconstructed using tracks.

The selection of events described above, where all multiplicity classes are included, will be denoted as V0M:0-100%.

[14]The PDG codes are given by the MC particle numbering scheme [42].

5.3 Reconstruction of K^0_s, Λ, and $\bar{\Lambda}$

The Λ, $\bar{\Lambda}$, and K^0_s decay weakly before reaching the detectors. Therefore, their detectable decay products were used when reconstructing the primary Λ, $\bar{\Lambda}$, and K^0_s candidates. The track selection for reconstructing $\Lambda(\bar{\Lambda})$ and K^0_s candidates was based on the V^0 decay topology, which will be explained in the next section.

The K^0_s meson is one of the two weak eigenstates of the neutral kaon system $K^0(d\bar{s})$ and $\bar{K}^0(s\bar{d})$. It has a mass of 497.611 MeV and a mean lifetime of 0.895×10^{-10} s [11]. The electrically neutral baryon Λ (uds) and its antiparticle $\bar{\Lambda}$ ($\bar{u}\bar{d}\bar{s}$) have the same mass of 1115.68 MeV and mean lifetime of 2.632×10^{-10} s [11]. In this analysis, the dominant decay channel for each of the three hadrons was used for the reconstruction. The dominant decay channels for the three hadrons are [11]

$$K^0_s \rightarrow \pi^+ + \pi^- \qquad BR : (69.20 \pm 0.05)\% \tag{5.3.1}$$

$$\Lambda \rightarrow p + \pi^- \qquad BR : (63.9 \pm 0.5)\% \tag{5.3.2}$$

$$\bar{\Lambda} \rightarrow \bar{p} + \pi^+ \qquad BR : (63.9 \pm 0.5)\% \tag{5.3.3}$$

The proton (p) has a positive electromagnetic charge, while its antiparticle ($\bar{p}$) is negatively charged.

5.3.1 The V^0 Decay Topology

Neutral unstable hadrons that manifest themselves by decaying into a pair of particles with opposite electromagnetic charges will produce a characteristic V-shape structure in the tracking detectors. The dominant decay channels of the K^0_s, Λ, and $\bar{\Lambda}$ demonstrate such decay topology and will from hereon be collectively referred to as the V^0 particles.

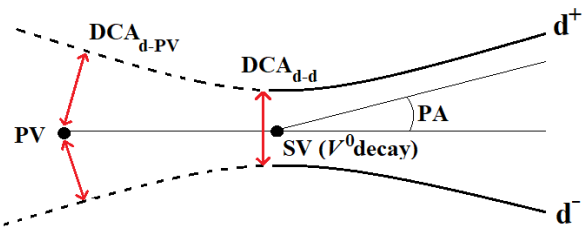

Figure 5.3.1: The V^0 decay topology. The figure illustrates three of the selection cuts used in this analysis, the distance of closest approach DCA_{d-PV} DCA_{d-d}, and the V^0 cosine of pointing angle PA.

Figure 5.3.1 demonstrates the V^0 decay topology. The V^0 particles created in the *primary vertex* (PV), i.e. the interaction point of the two beams, will travel a distance dependent on their lifetime and velocity before decaying. The point where the decay occurs creates a *second vertex* (SV) from which the charged decay products $d^{\pm}$ will propagate. The decay products of a V^0 particle will leave tracks in the detectors and their trajectories are then reconstructed in three-dimensional space. Through the trajectories of the decay products, it is possible to reconstruct the secondary vertices using a V^0 finder algorithm. In this analysis, the V^0 candidates were identified by the ALICE offline V^0 finder. An offline V^0 finder determines the V^0 vertices after the all tracks produced in the event have been reconstructed by a separate algorithm, while an online V^0 vertexer operates while simultaneously reconstructing the tracks. The charged tracks analyzed by the ALICE offline V^0 finder was reconstructed by the TPC and ITS.

The V^0 finder requires two tracks of opposite charge and the two tracks should appear from the same point in space if they originate from the same decay. To avoid false combinations, the distance of closest approach between the two daughter tracks ($\mathrm{DCA_{d-d}}$) at the secondary vertex has to be less than a given value. To exclude daughter tracks originating from the primary vertex, the distance of closest approach from the primary vertex to each of the two extended daughter tracks ($\mathrm{DCA_{d-PV}}$) has to be larger than a given value. There are several such requirements, or *cuts*, that can be applied to discard tracks that do not agree with the V^0 topology. All cuts applied to the reconstructed V^0 candidates in this analysis will be discussed in the next section.

Finally, the V^0 finder produces distributions in the form of a differential between the calculated invariant mass of the two combined tracks Δm_{V^0} and the known rest mass of the particle of interest ($m_{\mathrm{K^0_s}}$, m_Λ, and $m_{\bar{\Lambda}}$). For the three V^0 particles analyzed in this thesis, their corresponding Δm_{V^0} distributions are thus defined as follow

$$\Delta m_{\mathrm{K^0_s}} = m_{V^0} - m_{\mathrm{K^0_s}} \tag{5.3.4}$$

$$\Delta m_\Lambda = m_{V^0} - m_\Lambda \tag{5.3.5}$$

$$\Delta m_{\bar{\Lambda}} = m_{V^0} - m_{\bar{\Lambda}} \tag{5.3.6}$$

where the calculated invariant mass m_{V^0} of the two matching tracks is defined by Equation 3.1.3. For well selected $\mathrm{K^0_s}$ candidates, $m_{V^0} \rightarrow m_{\mathrm{K^0_s}}$ and the $\Delta m_{\mathrm{K^0_s}}$ distribution will have a peak around 0. Similarly, carefully chosen Λ and $\bar{\Lambda}$ candidates will generate clear peaks around 0 in their respective Δm_{V^0} distributions.

5.3.2 Selection of V^0 Candidates

All cuts applied to the V^0 selection are discussed in this section and they are summarized in Table 5.3.1. The cuts were evaluated by an MC analysis of the V0M:0-100% events before being applied on corresponding events from the real data. To assure full TPC acceptance, only daughter tracks and reconstructed V^0 candidates within $|\eta| < 0.8$ were accepted. The analysis was performed for V^0 candidates within the p_T interval 1.0-12.0 GeV/c. The following studies [14], [43], and [44] were used as a baseline for the selections explained below.

Table 5.3.1: Selections applied to the K^0_s, Λ, and $\bar{\Lambda}$ candidates.

Variable	Cut
Transverse Momentum Interval	1.0 GeV/c < p_T < 12.0 GeV/c
Pseudorapidity Interval for Daughter Tracks	$\lvert\eta_d\rvert < 0.8$
Pseudorapidity Interval for V^0 Candidates	$\lvert\eta_{V^0}\rvert < 0.8$
DCA: Daughter Tracks to PV ($DCA_{d\text{-}PV}$)	> 0.05 cm
DCA: Between V^0 Daughter Tracks at SV ($DCA_{d\text{-}d}$)	< 0.5 cm
V^0 Cosine of Pointing Angle (cosPA)	> 0.997
Transverse Decay Radius Interval	5 cm< r_{dec} < 100 cm
TPC PID Selection for Daughter Tracks	$\lvert n\sigma_{TPC}\rvert < 3$
Armenteros-Podolanski cut for K^0_s: p_T^{arm}	$> 0.2\lvert\alpha_{arm}\rvert$

Distance of Closest Approach: As mentioned in the previous section, the DCA_{d-PV} cut is applied in order to reject tracks originating from the primary vertex, while the DCA_{d-d} minimizes the risk of combining two daughter tracks that do not originate from the same decay. In this analysis, each daughter track had to have a DCA_{d-PV} greater than 0.05 cm to be accepted. Further, for two tracks to be accepted as a V^0 candidate, the distance between them, i.e. DCA_{d-d}, had to be smaller than 0.5 cm. The DCA_{d-PV} is given by the reconstructed tracks, while the DCA_{d-d} is calculated by the V^0 finder.

V^0 Cosine of Pointing angle: Through the V^0 finder, it is possible to check if the momentum of the V^0 candidate $\mathbf{p}_{V^0}$ points back to the primary vertex, which would be the case for a V^0 particle created in the primary vertex. The cosine of the angle between the momentum of the V^0 candidate $\mathbf{p}_{V^0}$ and a vector connecting the primary vertex with the secondary vertex is provided for each V^0 candidate, where $\mathbf{p}_{V^0}$ is calculated as the sum of the daughter track momenta. The angle is shown in Figure 5.3.1 as the pointing angle (PA). If the momentum of the V^0 candidate is overlapping with the vector connecting the primary vertex with the secondary vertex, then cos(PA)=1. In this analysis, only V^0 candidates with cos(PA)$>$ 0.997, which corresponds to an angle of $\sim 4.4^\circ$, were selected.

Transverse Decay radius: The distance between the primary vertex and the secondary vertices in the transverse plane has to be larger than 5 cm and less than 100 cm. This selection is obtained by requiring the transverse decay radius (r_{dec}) of the secondary vertex to be within that interval. A too short decay radius of the V^0 particle will make it difficult to separate a secondary vertex from a primary vertex. The requirement of $r_{dec} > 5$ cm will affect the K^0_s candidates more than the $\Lambda/\bar{\Lambda}$ candidates due to the shorter mean decay length $c\tau$, where τ is the mean lifetime. For K^0_s, $c\tau = 2.68$ cm, compared to $\Lambda/\bar{\Lambda}$ with $c\tau = 7.89$ cm. However, this will be corrected by the efficiency from the MC analysis. The efficiency is discussed in Section 5.5.1.

TPC PID: A substantial amount of combinatorial background was removed for Λ and $\bar{\Lambda}$ by a TPC PID criteria. Only V^0 candidates whose daughter tracks are within $\pm 3\sigma$ of the expected energy loss were accepted. The cut of $\lvert n\sigma_{TPC}\rvert < 3$ improves the PID of the proton and antiproton daughter tracks significantly, while the pion tracks are almost unaffected by the cut. Therefore, the yield of accepted K^0_s candidates did

not change substantially by this cut. With all the other cuts applied, the TPC PID cut discarded $\sim$ 2% of the K^0_s candidates, compared to $\sim$ 70% for Λ and $\bar{\Lambda}$, for $|\Delta m_{V^0}| \leq$ 0.04 GeV/c^2 and over the whole p_T range.

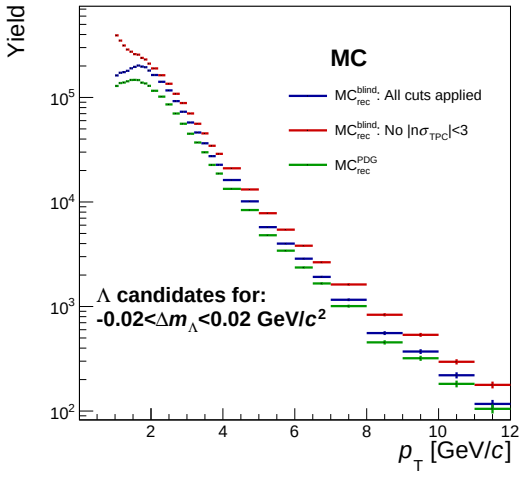

(a) The Λ yield from MC as function of p_T.

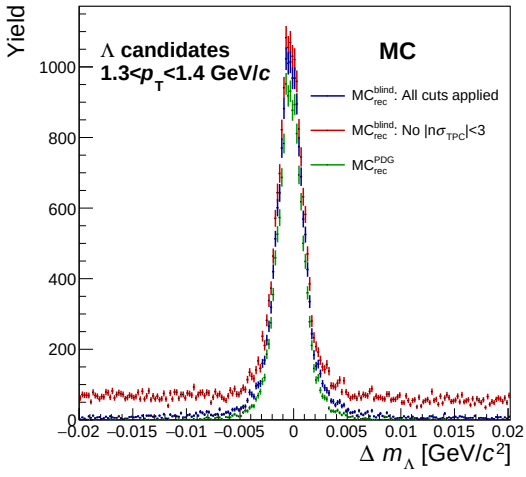

(b) The Δm_Λ distribution from MC in low p_T.

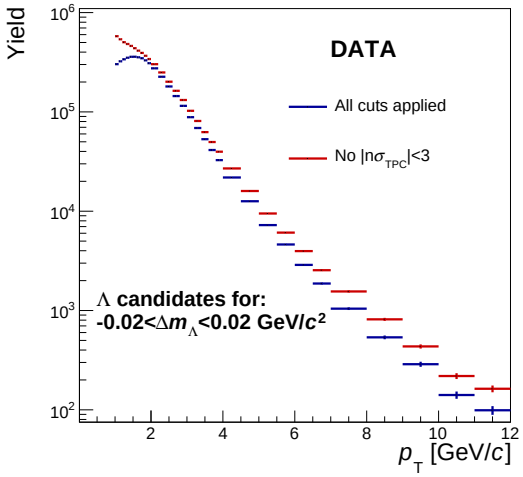

(c) The Λ candidates from data as function of p_T.

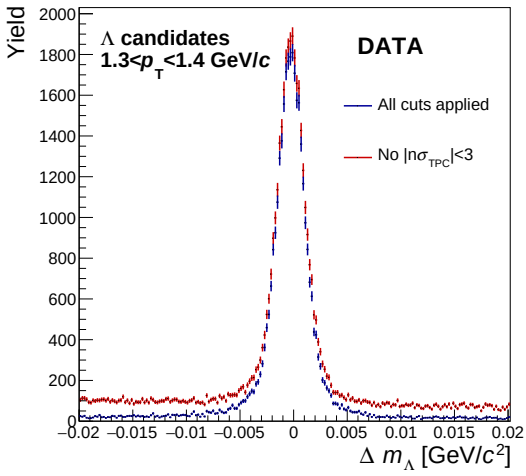

(d) The Δm_Λ distribution from data in low p_T.

Figure 5.3.2: The figures (a) and (b) show the Λ yield from MC$^{blind}_{rec}$ with all cuts applied (blue) and without the TPC PID cut of $|n\sigma_{\mathrm{TPC}}| < 3$ (red). This is compared to the Λ yield from MC$^{PDG}_{rec}$ (green). The figures (c) and (d) show Λ yield from data with all cuts applied (blue) and without the TPC PID cut (red). V0M:0-100% events are used for both MC and data.

The reliability of the effects when applying the cut was evaluated comparing the yields from MC$^{blind}_{rec}$, with and without the cut, to the true yield from MC$^{PDG}_{rec}$. In Figure 5.3.2(a) and (b), the MC analysis of the cut is shown. For (a), the Λ yield as a function of p_T normalized to the bin width is shown. The Λ candidates are obtained from the $-0.02 < \Delta m_\Lambda < 0.02$ GeV/c^2 intervals in each p_T-bin and the yield for

MC^{blind}_{rec} contains both signal and background. The effect of the $|n\sigma_{\mathrm{TPC}}| < 3$ cut is most pronounced at low p_{T} ($\lesssim 2$ GeV/c). Figure 5.3.2(b) shows the Δm_{Λ} distribution in the p_{T} interval of $1.3 - 1.4$ GeV/c. The cut reduces the background region significantly for MC^{blind}_{rec}. The shape of the MC^{blind}_{rec} yields before and after the cut is well reproduced in the real data, which is shown in Figure 5.3.2(c) and (d). The data yields in (c) and (d) were obtained in the same way as for the MC^{blind}_{rec} yields. By applying the cut on the data, combinatorial background is removed from the $\Lambda(\bar{\Lambda})$ distributions without loosing a significant part of the peak. The cut generates similar effects for the $\bar{\Lambda}$ yields from MC^{blind}_{rec} and data, which are shown in Appendix A.

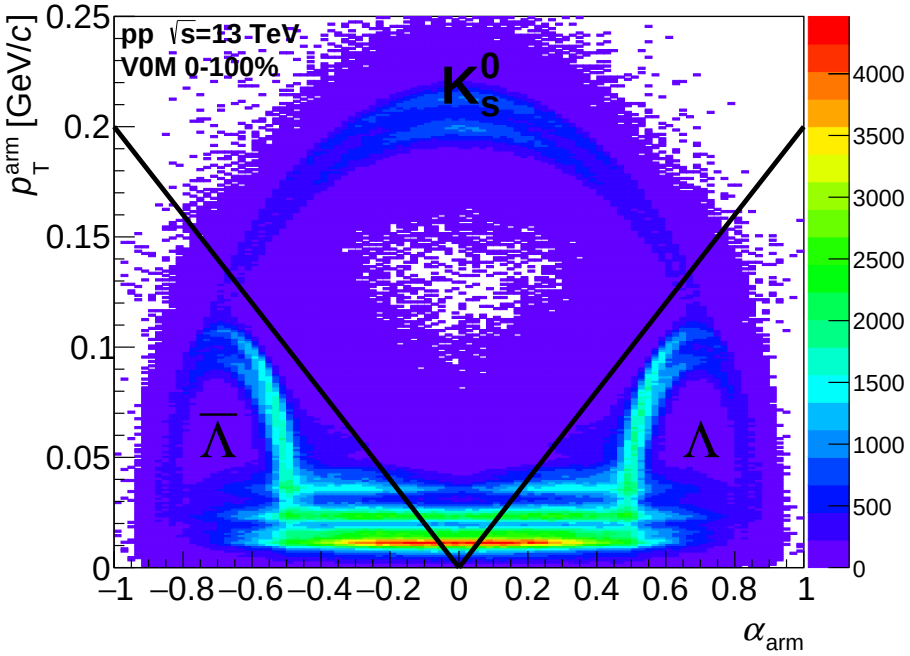

Figure 5.3.3: The Armenteros-Podolanski Diagram produced from data. The different areas in which the V^0 species cluster are marked with K^0_s, Λ, and $\bar{\Lambda}$. The p_{T}^{arm} cut for K^0_s is demonstrated by the black line.

Armenteros-Podolanski Diagram: A selection on the Armenteros-Podolanski diagram was made only for K^0_s candidates with the purpose to remove Λ and $\bar{\Lambda}$ candidates misidentified as K^0_s particles. Figure 5.3.3 illustrates the kinematic properties of the V^0 particles. The two-dimensional plot shows the transverse momentum of the positively charged daughter p_{T}^{arm} tracks with respect to the V^0 particle as a function of the longitudinal momentum asymmetry of the daughter tracks α_{arm}. The p_{T}^{arm} and α_{arm} variables are defined as [45]

$$p_{\mathrm{T}}^{arm} = \frac{|\mathbf{p}_{\mathrm{T}}^{+} \times \mathbf{p}_{V^0}|}{|\mathbf{p}_{V^0}|} \qquad \alpha_{arm} = \frac{p_L^{+} - p_L^{-}}{p_L^{+} + p_L^{-}} \tag{5.3.7}$$

where $\mathbf{p}_{\mathrm{T}}^{+}$ is the transverse momentum vector for the positively charged daughter particle and $\mathbf{p}_{V^0}$ is the three-momentum of the V^0 (mother) particle. Further, the $p_L^{\pm}$

is the longitudinal momentum of the daughter tracks relative to the direction of the V^0 mother particle. The distribution obtained in this analysis is shown in Figure 5.3.3. The decay products of K_s^0 are charged pions, which have the same mass. Therefore, their momenta will be distributed symmetrically on average giving rise to the K_s^0 area in Figure 5.3.3. For the decays of Λ and $\bar{\Lambda}$, the proton and antiproton will take larger parts of the momenta giving rise to the two asymmetrical distributions demonstrated in Figure 5.3.3. By applying a cut where only K_s^0 candidates with $p_T^{arm} > 0.2|\alpha_{arm}|$ are accepted, the Λ and $\bar{\Lambda}$ candidates misidentified as K_s^0 can be removed.

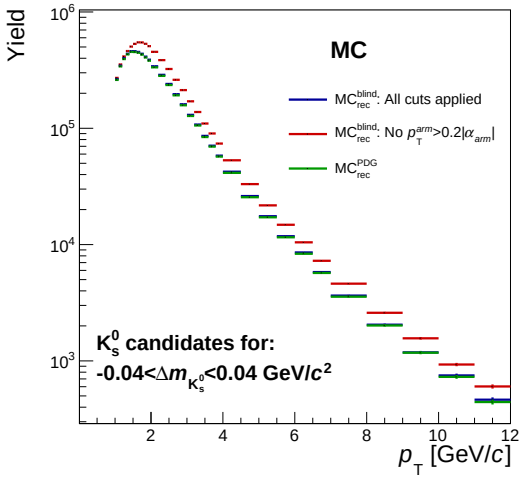

(a) The K_s^0 candidates as function of p_T.

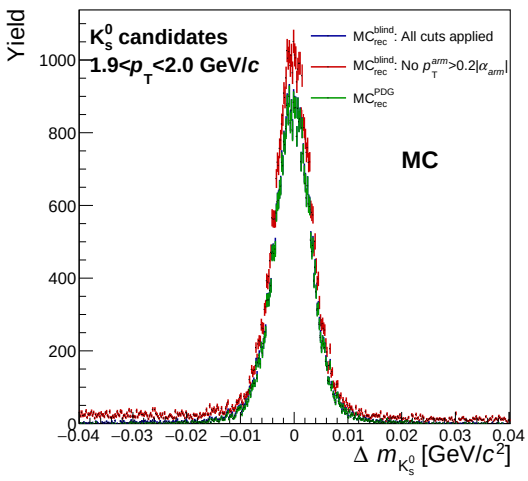

(b) The $\Delta m_{K_s^0}$ distribution in low p_T.

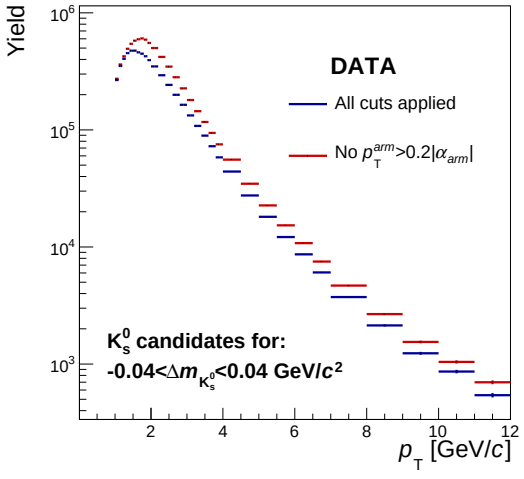

(c) The K_s^0 candidates as function of p_T.

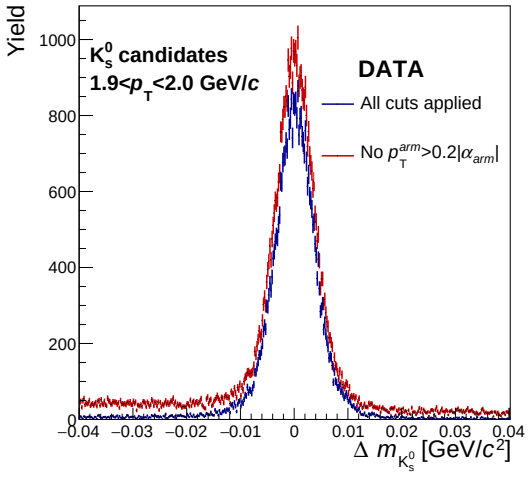

(d) The $\Delta m_{K_s^0}$ distribution in low p_T.

Figure 5.3.4: The figures (a) and (b) show the K_s^0 yield from MC_{rec}^{blind} with all cuts applied (blue) and without the p_T^{arm} cut (red). This is compared to the K_s^0 yield from MC_{rec}^{PDG} (green). The figures (c) and (d) show K_s^0 yield from data with all cuts applied (blue) and without the p_T^{arm} cut (red). V0M:0-100% events are used for both MC and data.

The effect of the cut on the K^0_s yield from MC^{blind}_{rec} is shown in Figure 5.3.4(a) and (b). In (a), the K^0_s yield as a function of p_T is obtained by integrating the $-0.04 < \Delta m_{K^0_s} < 0.04$ GeV/c^2 intervals in each p_T-bin, which is normalized to the bin width. Therefore, the MC^{blind}_{rec} contains both signal and background. In (b), the $\Delta m_{K^0_s}$ distribution in the p_T interval of $1.9 - 2.0$ GeV/c is shown. The MC^{blind}_{rec} with and without the cut is compared to the true yield from MC^{PDG}_{rec}. Similarly, the K^0_s yields from real data are shown in Figure 5.3.4(c) and (d), where the data exhibits the same effect of the cut as for MC^{blind}_{rec}. Figure 5.3.4(b) and (d) demonstrates a reduction of both the background and the peak.

5.4 Signal Extraction

The raw signals of the V^0 particles were obtained by studying their corresponding Δm_{V^0} distributions as a function of the p_T, within the range $1.0 < p_T < 12.0$ GeV/c. The signals were extracted from the Δm_{V^0} distribution in each p_T-bin. The signal extraction was done by first defining the peak width in each p_T-bin by the truncated mean method, and then removing the background from the peak region by the sideband subtraction method. The signal and background of K^0_s, Λ, and $\bar{\Lambda}$ were estimated for V0M:0-100% events.

5.4.1 The Truncated Mean Method

The peak regions were defined by first determining the spread of the Δm_{V^0} peak in each p_T-bin. If each Δm_{V^0} distribution has a clear peak, the width can be obtained by a suitable fit that describes the peak. However, the Δm_{V^0} distributions in the high p_T-bins ($\gtrsim 8$ GeV/c) do not have clear peaks. Aside from the low statistics in the p_T-bins, the relative error $\Delta p/p$ of the measurement of high-p_T particles is larger than for low-p_T particles generating less defined peaks in the high p_T region. Therefore, fits are not used when extracting the signals from the Δm_{V^0} distributions obtained from data.

In order to do good estimations of the peak regions over the whole p_T range, the truncated mean method was applied. The method discards the high and low ends of a probability distribution with the purpose of statistically measuring the central tendency. To avoid the risk of removing a significant part of the V^0 signal by making the Δm_{V^0} distribution too narrow, the simulated MC^{PDG}_{rec} data was studied for each V^0 particle before truncating the Δm_{V^0} distributions obtained from real data. A minimum Δm_{V^0} range estimation using the MC^{PDG}_{rec} was performed by fitting a double Gaussian to a wide Δm_{V^0} range. Figure 5.4.1 panels (a), (c), and (e) show the Δm_{V^0} distributions obtained from MC^{PDG}_{rec} with the double Gaussian fits (red line). Each fit returns the standard deviation[15] σ_{MC} and integrating over a peak region slightly larger than $\pm 6\sigma_{MC}$ yields the major part of the signal, 99+% of the total number of candidates in the Δm_{V^0} range for all V^0 particles. This minimum Δm_{V^0} range estimation for each V^0 particle was then applied on real data, resulting in the truncated range $|\Delta m_{K^0_s}| \leq 0.02$ GeV/c^2 for K^0_s candidates and $|\Delta m_{\Lambda/\bar{\Lambda}}| \leq 0.008$ GeV/c^2 for Λ and $\bar{\Lambda}$ candidates.

[15] The fits return $\sigma_{MC} \approx 0.0033$ GeV/c^2 for K^0_s, and $\sigma_{MC} \approx 0.0012$ GeV/c^2 for Λ and $\bar{\Lambda}$.

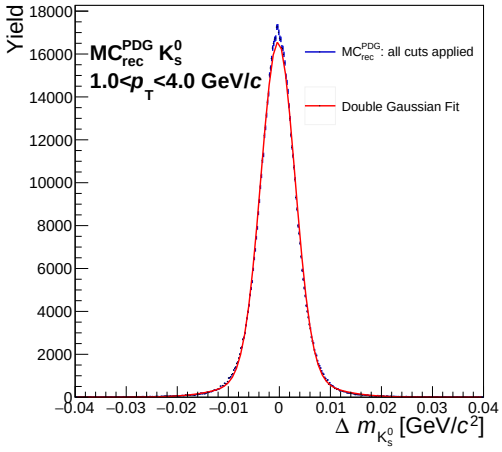

(a) The K^0_s yield used for double Gaussian fit.

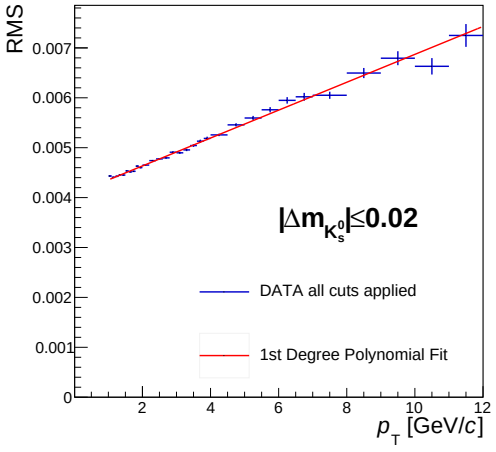

(b) The K^0_s RMS as a function of p_T.

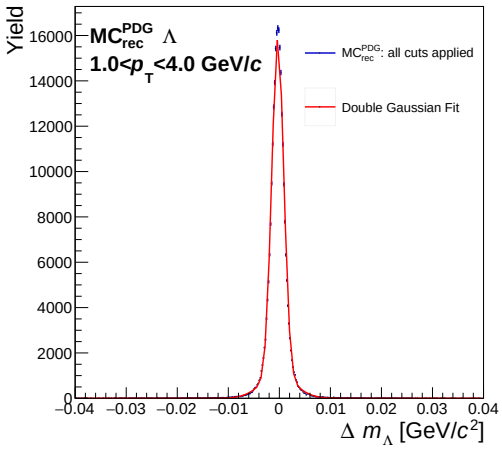

(c) The Λ yield used for double Gaussian fit.

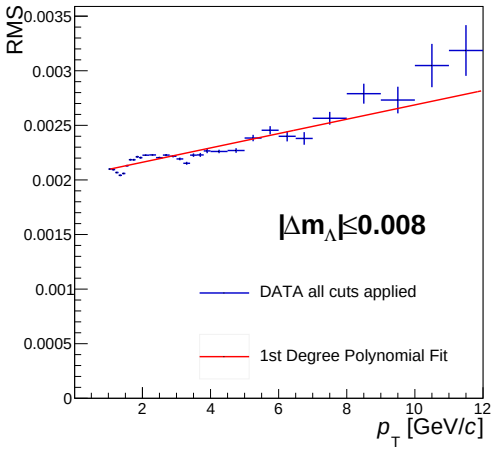

(d) The Λ RMS as a function of p_T.

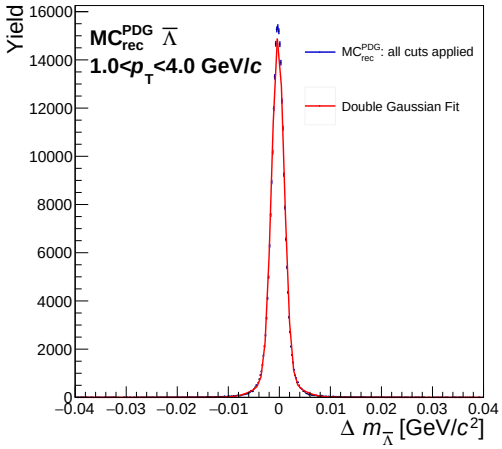

(e) The $\bar{\Lambda}$ yield used for double Gaussian fit.

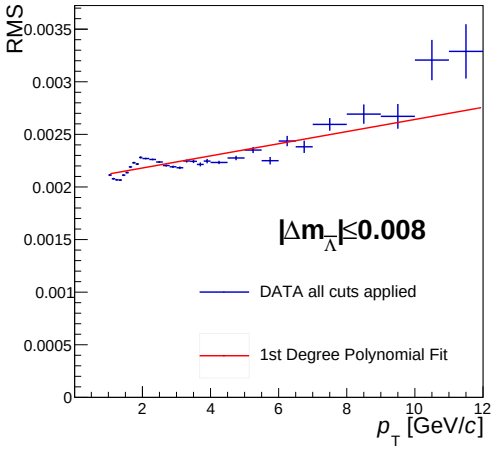

(f) The $\bar{\Lambda}$ RMS as a function of p_T.

Figure 5.4.1: The Δm_{V^0} distributions from MC$^{PDG}_{rec}$ used for double Gaussian fits (left). The RMS dependence of p_T when applying the truncated mean method to data (right). V0M:0-100% events are used for both MC and data.

Data was used when estimating the width of the peaks in each p_{T}-bin. The truncated Δm_{V^0} distributions yield a root-mean-square (RMS) value, dependent on the p_{T}. The RMS as a function of p_{T} for each V^0 particle is shown in Figure 5.4.1(b),(d), and (f). A first degree polynomial is fitted for each RMS vs. p_{T} distribution to reduce the effects generated by statistical fluctuations and combinatorial background. Each truncated distribution also yields a mean value. This value, which is dependent on every entry in the distribution whether it is a true V^0 particle or background, is close to zero ($\sim 0 \pm 4 \times 10^{-4}$ GeV/c^2) for p_{T} up to 10 GeV/c. Therefore, the mean value is set to zero, which corresponds to the ideal selection of V^0 candidates. When the mean of a peak is zero, the definition of the RMS and of the standard deviation are the same and the RMS will be denoted as σ from here on. The standard deviations σ obtained from the fitted RMS should not be confused with σ_{MC}, which was only used for estimating the minimum range for the truncated Δm_{V^0} distributions. The σ value obtained from the polynomial fit for each p_{T}-bin is used when extracting the V^0 signals and estimating the background, which will be discussed in the next section.

5.4.2 The Sideband Subtraction Method

If the background exhibits an approximately linear behavior within a region surrounding the peak, it is plausibly also approximately linear in the peak region. By assuming a linear background for a considered region, the sideband subtraction method can be used for removing the background from the signal. This is done by first defining a peak region and on each side of the peak region, two background regions, called the sidebands. The sum of the sideband interval widths is the same size as the peak region. The background estimate is then removed from the peak region by integrating the two sideband regions and subtracting the areas from the integrated peak region.

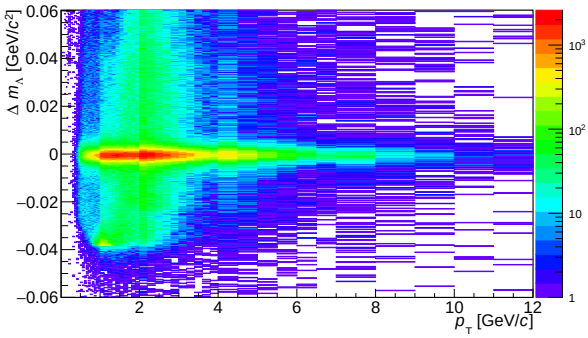

(a) The Λ signal and background yield from data with all cuts applied.

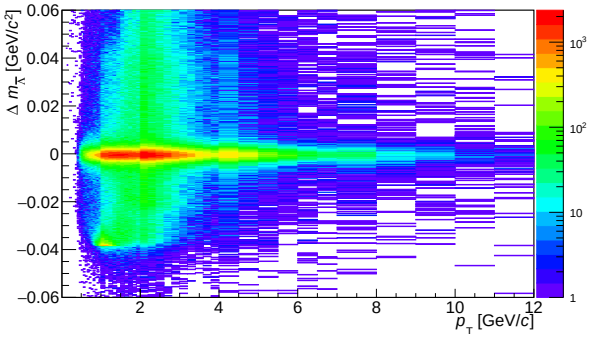

(b) The $\bar{\Lambda}$ signal and background yield from data with all cuts applied.

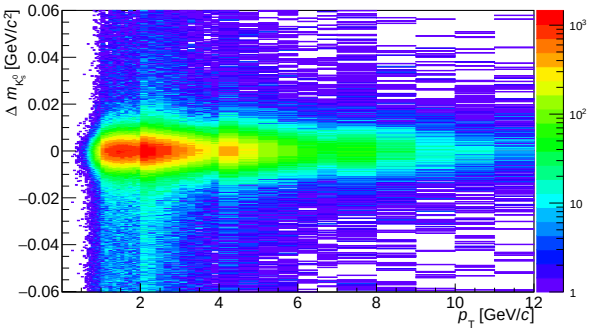

(c) The K^0_S signal and background yield from data with all cuts applied.

Figure 5.4.2: The Δm_{V^0} distributions as a function of p_T for each V^0 particle from V0M:0-100% events (real data) with all cuts applied.

Ideally, an overestimation of the true peak region would not affect the size of the extracted signal as long as the background is linear. Figure 5.4.2 shows the Δm_{V^0} distributions as a function of p_T. At low p_T (< 4.0 GeV/c), the Δm_{V^0}distributions demonstrate tails at the end parts and at high p_T, the statistics decreases rapidly. Therefore, the peak region was defined as $\pm 3\sigma$ to assure background linearity and this cut should still include $\sim 99.73\%$ of the signal.

A peak region and two sidebands were defined for the Δm_{V^0} distributions in each p_T-bin. For each V^0 particle, the peak region was defined as $[-3\sigma,3\sigma]$, and the two sidebands as $[-6\sigma,-3\sigma]$ and $[3\sigma,6\sigma]$, where the V^0 particle's associated σ in each p_T-bin is obtained from the first degree polynomials in Figure 5.4.1(b),(d), and(f). Figure 5.4.3 shows the two sidebands and the peak region for each V^0 particle at a low p_T interval of $1.9 - 2.0$ GeV/c and at a high interval of $7.0 - 8.0$ GeV/c. The low statistics at $p_T > 8.0$ GeV/c makes it difficult to observe linearity of background. However, by choosing the truncated mean method instead of a fit, the low statistic will not affect the signal extraction significantly and the method can be assumed to hold at high p_T as well.

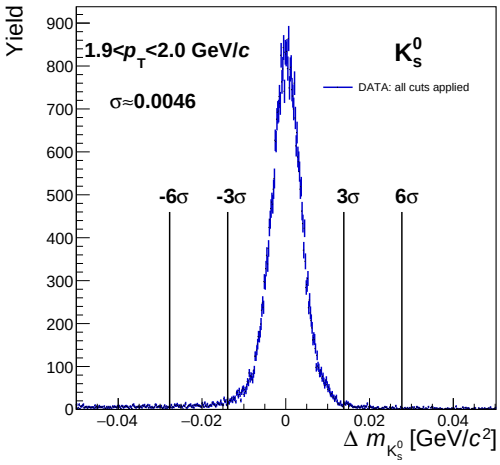

(a) Sideband subtraction for K^0_S at low p_T.

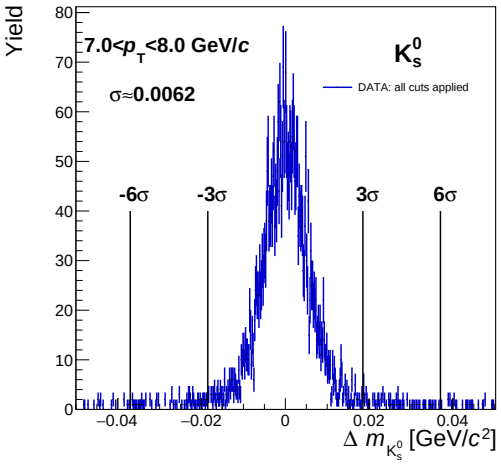

(b) Sideband subtraction for K^0_S at high p_T.

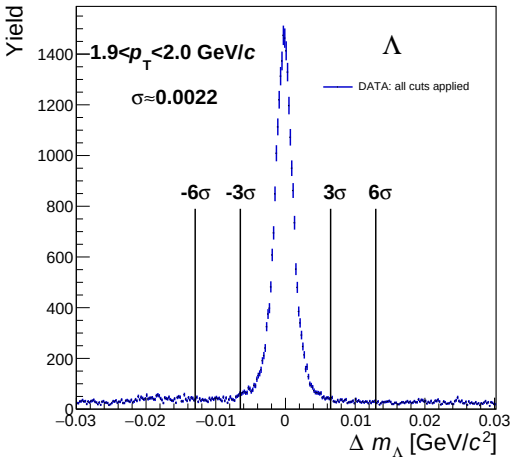

(c) Sideband subtraction for Λ at low p_T.

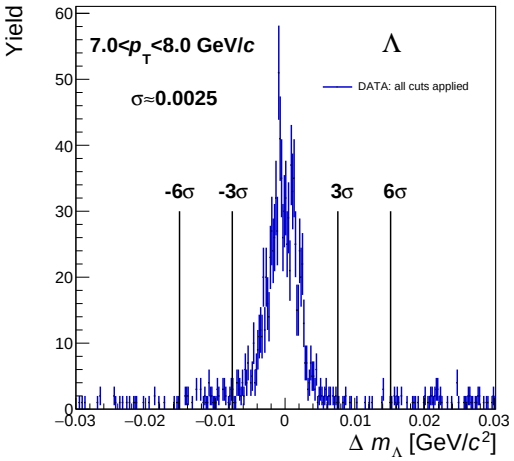

(d) Sideband subtraction for Λ at high p_T.

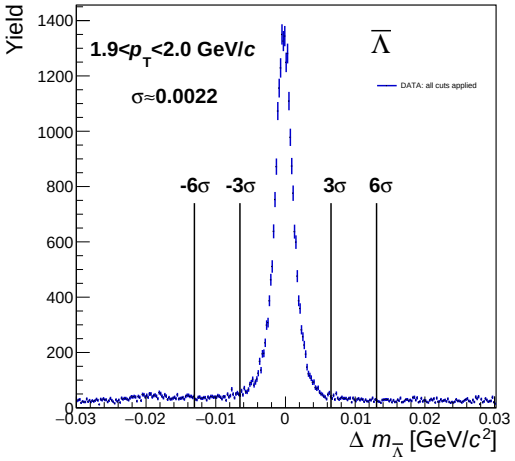

(e) Sideband subtraction for $\bar{\Lambda}$ at low p_T.

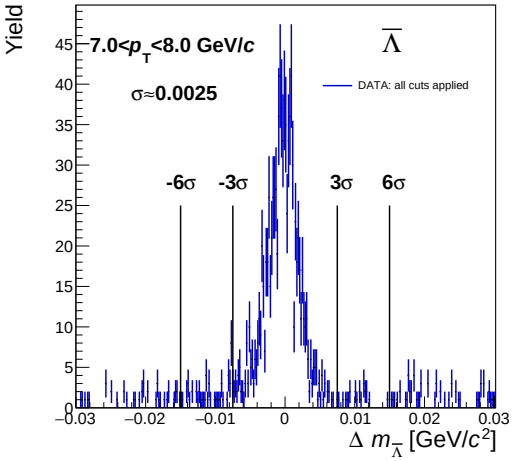

(f) Sideband subtraction for $\bar{\Lambda}$ at high p_T.

Figure 5.4.3: The extraction of V^0 signals by the sideband subtraction method. The Δm_{V^0} distributions are from V0M:0-100% events.

5.5 Corrections to the p_{T}-spectra

From the V^0 selection (the cuts) and the extraction of the signals, the uncorrected p_{T}-spectra are obtained. Figure 5.5.1 shows the p_{T}-spectra of the V^0 particles for real data, $\mathrm{MC}_{rec}^{blind}$, and MC_{rec}^{PDG}, where both data and $\mathrm{MC}_{rec}^{blind/PDG}$ have passed the V^0 selection. For real data and $\mathrm{MC}_{rec}^{blind}$, the backgrounds were subtracted from the peak regions when extracting the signals. While for MC_{rec}^{PDG}, which do not have combinatorial background, the signal was obtained by extracting the peak region without background subtraction. The number of V^0 candidates N are normalized to the number of analyzed events (N_{ev}), i.e. that passed the event selection defined in Section 5.2, and the p_{T}-bin widths ($\mathrm{d}p_{\mathrm{T}}$).

The uncorrected p_{T}-spectra obtained from real data are compared to the corresponding spectra from MC data. There is a discrepancy between the MC data and the real data for Λ and $\bar{\Lambda}$, where the MC simulated data seem to underestimate the number of particles. It has been observed that PYTHIA underestimates the production of strange particles, and that the discrepancy grows with increasing particle mass and strangeness content [43, 46, 47]. However, the shapes are similar and by assuming that the MC analysis approximately agrees with the data analysis for the V0M:0-100% event selection, the efficiency and feeddown corrections can be calculated by the MC analysis and then applied on data. Additionally, the p_{T}-spectra will be corrected by choosing a rapidity window Δy. The final p_{T}-spectra will then be

$$\frac{1}{N_{\mathrm{ev}}}\frac{\mathrm{d}^2N}{\mathrm{d}p_{\mathrm{T}}\mathrm{d}y} = \frac{S}{N_{\mathrm{ev}}} \times \frac{1}{\Delta p_{\mathrm{T}}} \times \frac{1}{\Delta y} \times \frac{1}{\text{Efficiency}} \times feeddown(\Lambda, \bar{\Lambda}) \tag{5.5.1}$$

where S is the extracted signal for each V^0 particle. Only Λ and $\bar{\Lambda}$ yields are corrected for the $feeddown$, which is discussed in Section 5.5.2. The computed corrections are applied on the final V^0 yields for the V0M:0-100% events, the high multiplicity events and the events selected by spherocity cuts. The selections of the high multiplicity events and spherocity events will be defined in Section 5.6 and 5.6.1, respectively.

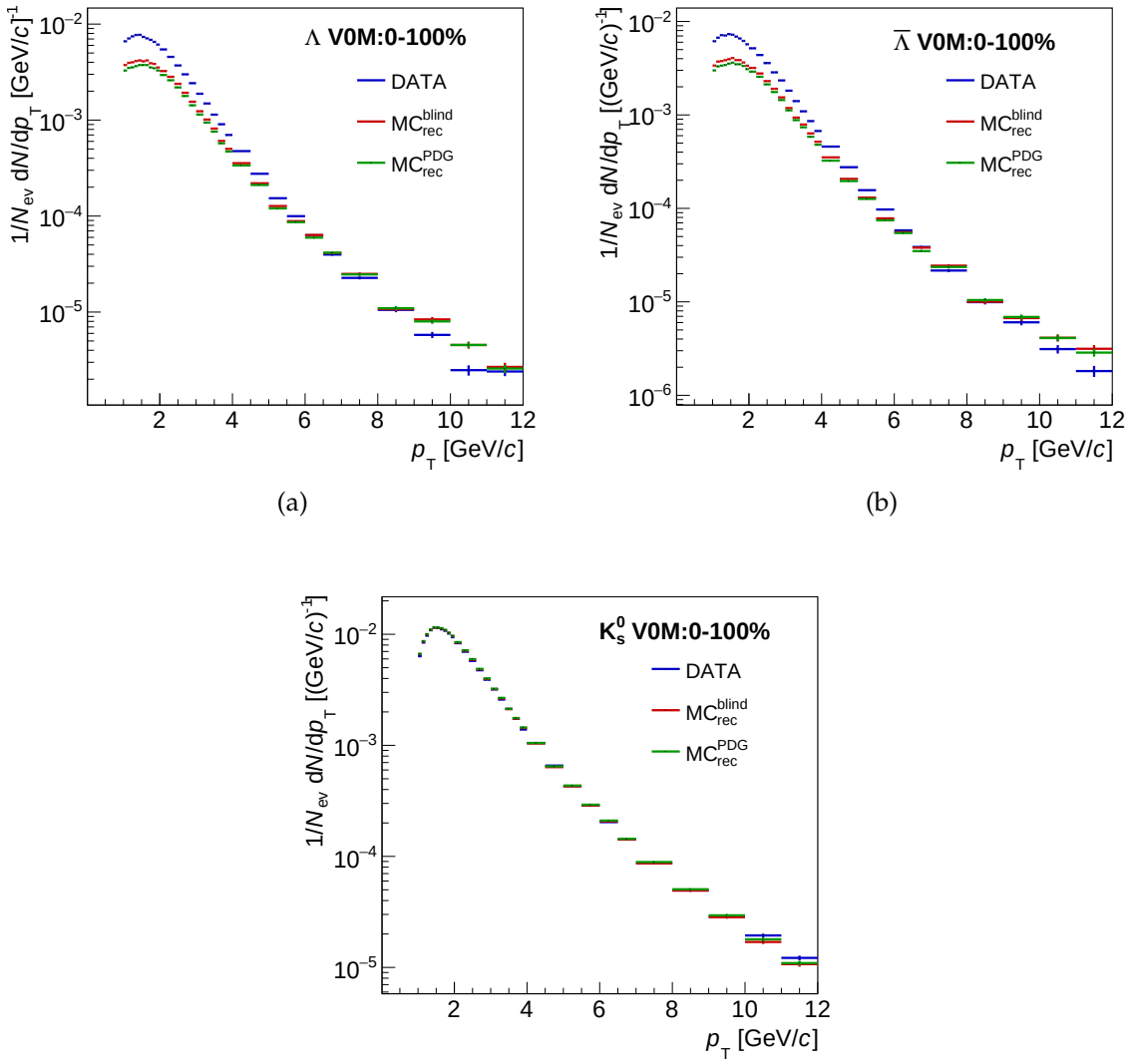

Figure 5.5.1: The uncorrected p_{T}-spectra for Λ (a), $\bar{\Lambda}$ (b), and K_s^0 (c). The MC analysis is compared to the data analysis.

5.5.1 Efficiency

The performance of the detector, albeit good, is not perfect and therefore, efficiency correction factors are computed for each V^0 particle. The efficiency corrects the p_{T}-spectra for the imperfections when reconstructing particles and the V^0 signal loss when applying cuts. The efficiency for the associated V^0 particle is computed in each p_{T}-bin by the ratio

$$\text{Efficiency} = \frac{\mathrm{MC}_{rec}^{PDG}(V^0)}{\mathrm{MC}_{gen}^{PDG}(V^0)} \tag{5.5.2}$$

where MC^{PDG}_{rec} data is required to be primary V0 particles originating from the same decay channels and pass the same selections as in the data analysis. The MC^{PDG}_{gen} data is the primary V^0 particles created in each event, before passing through the detector simulation and V^0 particles from MC^{PDG}_{gen} is required to be within $\mid \eta \mid < 0.8$. In Figure 5.5.2, the efficiency for the V^0 particles for the MC analysis (V0M:0-100%) is shown.

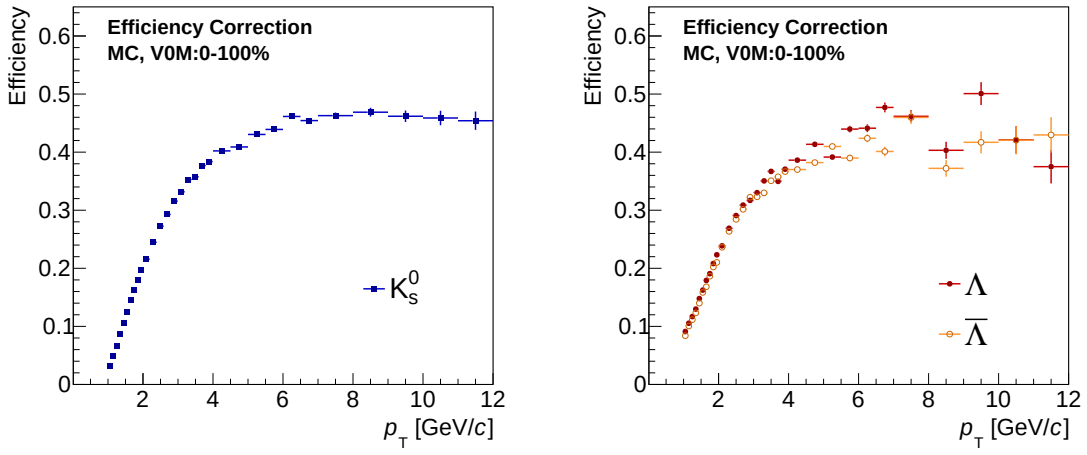

(a) (b)

Figure 5.5.2: The K^0_s (a) efficiency and the Λ and $\bar{\Lambda}$ efficiencies (b).

5.5.2 Feeddown Subtraction for Λ and $\bar{\Lambda}$

The measured Λ and $\bar{\Lambda}$-spectra are sums of primary and secondary Λ and $\bar{\Lambda}$ particles. The main contribution of secondary Λ particles to the Λ-spectrum is the feeddown from the multi-strange particle Ξ^- (Ξ^+ for $\bar{\Lambda}$), which has the main decay channel $\Xi^- \rightarrow \Lambda + \pi^-$. Other multi-strange particles contributing to the Λ and $\bar{\Lambda}$-spectra are $\Omega^{\pm}$ and Σ^0. There is no significant decay contributing to secondary K^0_s particles and therefore, no feeddown correction was done for the K^0_s-spectrum.

To remove the secondary Λ and $\bar{\Lambda}$ from the measured p_T-spectra, the number of secondaries was estimated using the MC^{PDG}_{rec} sample. The primary Λ ($\bar{\Lambda}$) yield and the total Λ ($\bar{\Lambda}$) yield, i.e. including both primaries and secondaries, can be given using the MC^{PDG}_{rec} data sample. The feeddown was obtained from the ratio of the primary Λ ($\bar{\Lambda}$) yield to the total Λ ($\bar{\Lambda}$) yield. The fraction of secondary Λ and $\bar{\Lambda}$ removed from the p_T-spectra is shown in Figure 5.5.3.

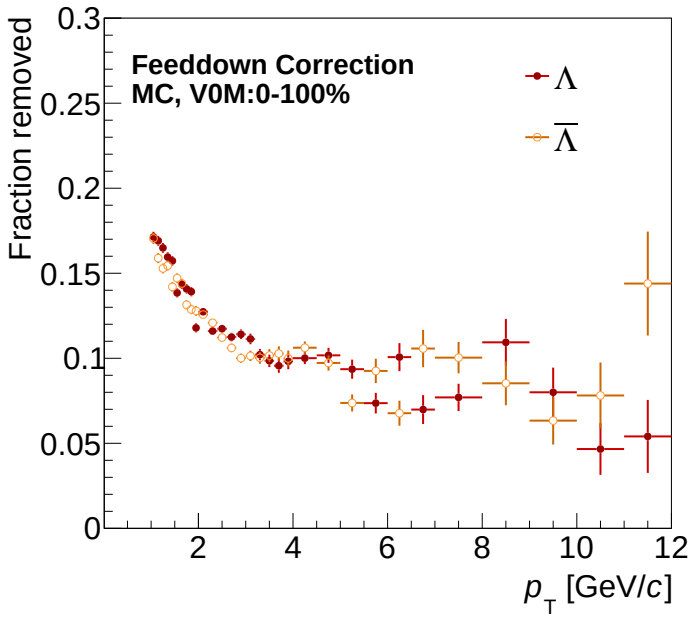

Figure 5.5.3: The feeddown fractions removed from the Λ and $\bar{\Lambda}$ yields.

5.5.3 The Rapidity Window

The rapidity distribution for K^0_s, Λ and $\bar{\Lambda}$ in Figure 5.5.4 shows that, as expected, the acceptance decreases in the ends of the detector, $y \rightarrow \pm 0.8$, both for MC data and real data. The rapidity interval $\mid y \mid < 0.7$, which discards the end parts of the detector, was chosen for the analysis and it corresponds to the rapidity window Δy=1.4.

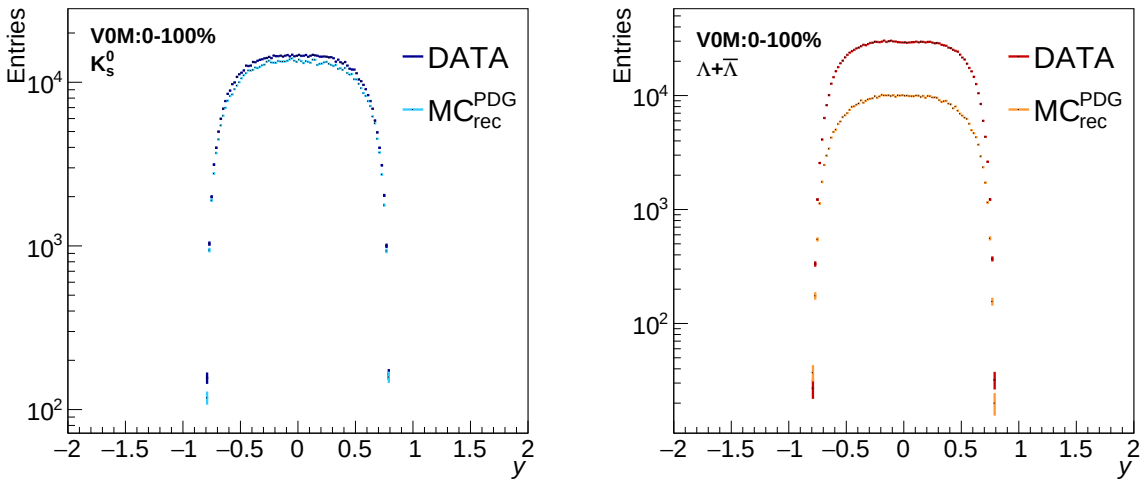

(a) (b)

Figure 5.5.4: The rapidity for K^0_s (a) and Λ and $\bar{\Lambda}$ (b).

5.6 High Event Multiplicity Selection

The events used for the high multiplicity analysis (V0M:0-10%) had to pass the selections listed in the Section 5.2. In addition to that, only the 10% events out of the total real data set that generate the highest VZERO amplitudes are accepted, i.e. the top 10% highest multiplicity events are selected. The events passing this selection will be referred to as the high multiplicity events or denoted as V0M:0-10%.

5.6.1 Event Shape Analysis by Spherocity Cuts

The high multiplicity events were used for further selections in an attempt to separate jetty events from isotropic events using the transverse spherocity, which is explained and defined in Section 3.4. The high multiplicity events accepted for the spherocity analysis were required to have at least 10 tracks within the mid-pseudorapidity range of $|\eta|$<0.8.

Two selection cuts were applied on the events accepted for the spherocity analysis. The 20% of the accepted spherocity events with the highest spherocity values were selected as the isotropic events, $S_O > 0.76$. Similarly, the 20% with the lowest spherocity values were selected as the jetty events, $S_O < 0.47$. Figure 5.6.1 shows the total distribution of accepted events as a function of the spherocity. The figure also demonstrates the 20% events selected as jetty and the 20% events selected as isotropic, the events are shown in red and blue, respectively.

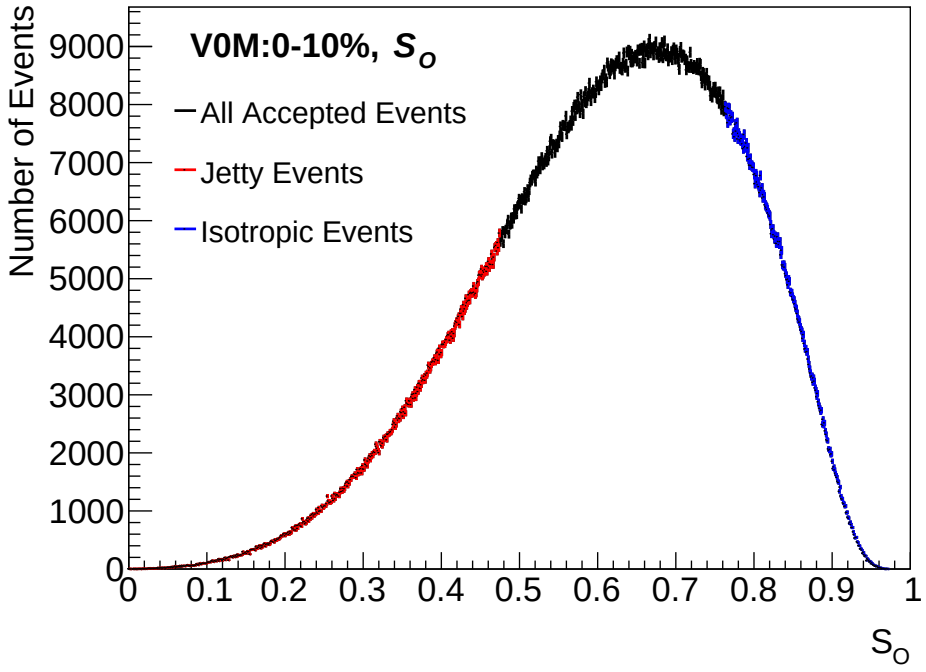

Figure 5.6.1: The spherocity of all the accepted events (black), the 20% events yielding lowest spherocity(red), and the 20% events yielding the highest spherocity (blue).

5.7 Statistical Uncertainties

The statistical uncertainties for the extracted signals were estimated by the propagation of error formula [48]. For a function f that depends on two variables, x and y, the error σ_f is

$$\sigma_f \simeq \left(\frac{\delta f}{\delta x}\right)^2 \sigma_x^2 + \left(\frac{\delta f}{\delta y}\right)^2 \sigma_y^2 + 2\mathrm{cov}(x,y)\frac{\delta f}{\delta x}\frac{\delta f}{\delta y} \tag{5.7.1}$$

The integrated peak region contains both the number of signal entries S and background entries B, and the two sidebands the background entries B_{side}. By setting $x = B + S$ and $y = B_{side}$ in the equation above, it is clear that x and y are independent in each p_{T}-bin and thus, the covariance is equal to zero. Hence, the error for the extracted signal σ_s in each p_{T}-bin is

$$\sigma_s = \sqrt{(B+S)^2 + B_{side}^2} \tag{5.7.2}$$

The statistical uncertainties for the efficiencies and the feeddowns were estimated by the binomial error [48]. For n trials and m successes, the efficiency p is estimated as $p = m/n$, and the error of p is

$$\sigma_p = \sqrt{\frac{p(1-p)}{n}} \tag{5.7.3}$$

In the same way, the errors for the feeddowns were calculated.

6 Results

In this thesis, the three strange hadrons K^0_s, Λ, and $\bar{\Lambda}$ were reconstructed via their V^0 decay topology and their respective particle production as a function of transverse momentum p_{T} are studied for events with no multiplicity bias (V0M:0-100%) and for high multiplicity events (V0M:0-10%). Further, the p_{T}-spectra of the three hadrons are studied for two types of high multiplicity events whose shapes been characterized by the transverse spherocity, i.e. low spherocity events and high spherocity events.

This chapter presents the results in two sections. First, the p_{T}-spectra of K^0_s, Λ, and $\bar{\Lambda}$ for the different event selections are presented. The event selections performed are defined in Section 5.2, 5.6, and 5.6.1. In the second part, the results of the baryon-to-meson ratios, $(\Lambda + \bar{\Lambda})/2\mathrm{K}^0_s$, for the different event selections are presented.

6.1 The K^0_s, Λ, and $\bar{\Lambda}$ Yields

The K^0_s, Λ, and $\bar{\Lambda}$ particle productions in pp collisions at $\sqrt{s}$=13 TeV as a function of p_{T} are shown in Figures 6.1.1, 6.1.2, and 6.1.3, respectively. The figures demonstrate the event multiplicity and event shape dependence of the particle productions. The p_{T}-spectra obtained from events with no multiplicity bias (V0M:0-100%) and high multiplicity events (V0M:0-10%) are shown in (a), and the p_{T}-spectra obtained from high

multiplicity events (V0M:0-10%) with low spherocity $S_O < 0.47$ and high spherocity $S_O > 0.76$ are shown in (b).

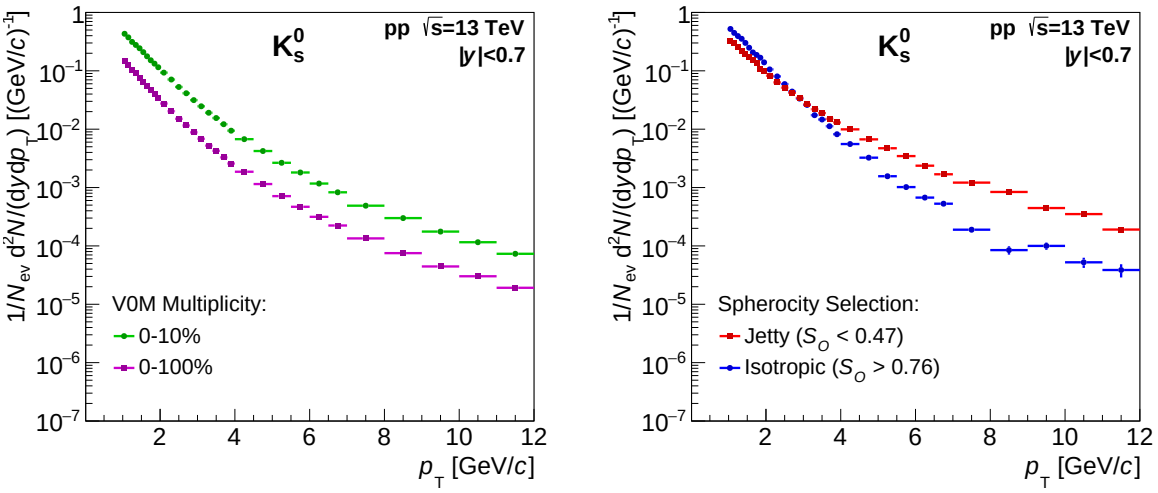

(a) (b)

Figure 6.1.1: The K^0_s p_T-spectra for the event selections. The p_T-spectra for events with no multiplicity bias (V0M:0-100%) and for high multiplicity events (V0M:0-10%) are shown in (a). The p_T-spectra for high multiplicity events (V0M:0-10%) with two additional spherocity cuts are shown in (b).

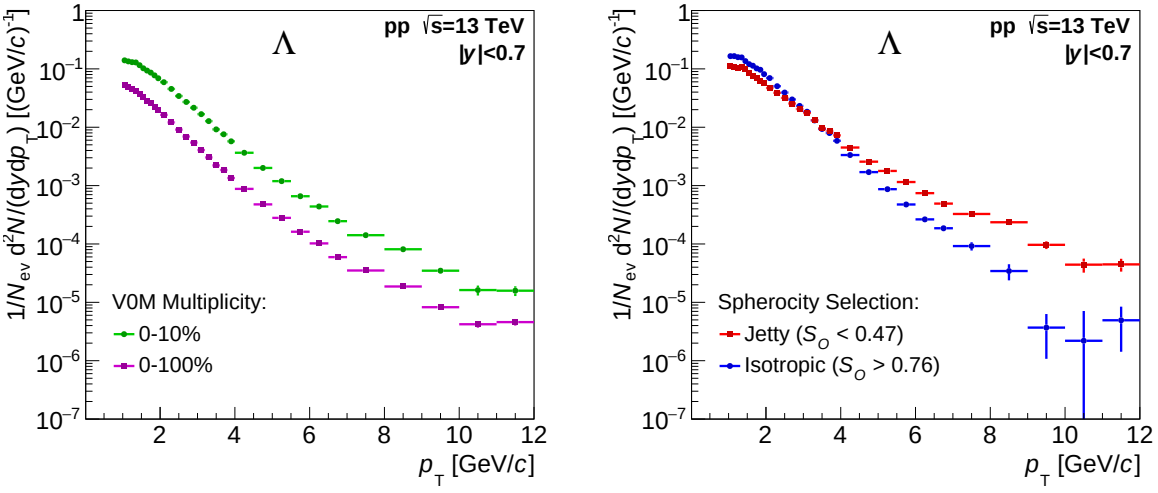

(a) (b)

Figure 6.1.2: The Λ p_T-spectra for the event selections. The p_T-spectra for events with no multiplicity bias (V0M:0-100%) and for high multiplicity events (V0M:0-10%) are shown in (a). The p_T-spectra for high multiplicity events (V0M:0-10%) with two additional spherocity cuts are shown in (b).

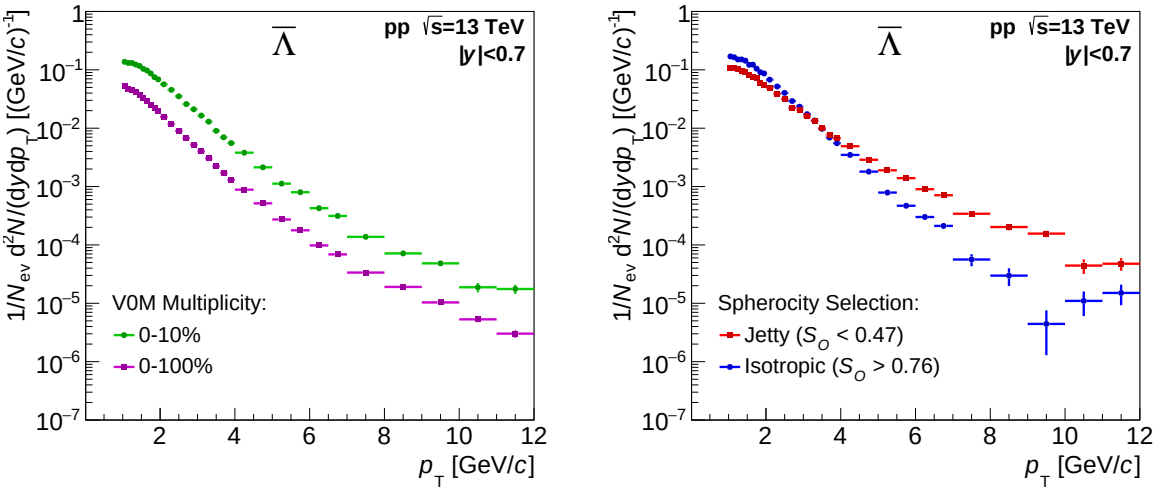

(a) (b)

Figure 6.1.3: The $\bar{\Lambda}$ p_{T}-spectra for the event selections. The p_{T}-spectra for events with no multiplicity bias (V0M:0-100%) and for high multiplicity events (V0M:0-10%) are shown in (a). The p_{T}-spectra for high multiplicity events (V0M:0-10%) with two additional spherocity cuts are shown in (b).

6.2 The Baryon-to-Meson Ratio

The baryon-to-meson ratios $(\Lambda + \bar{\Lambda})/2\mathrm{K}^0_s$ are shown in Figure 6.2.1. The sum of the Λ and $\bar{\Lambda}$ p_{T}-spectra is divided by the K^0_s p_{T}-spectrum, which is multiplied by a factor two. The ratios in Figure 6.2.1 have a wider p_{T}-binning and a slightly reduced p_{T} interval of 1.0-11.0 GeV/c, where the high-p_{T} yield (>11.0 GeV/c) have been discarded. In (a), the ratios for the p_{T}-spectra obtained from events with no multiplicity bias (V0M:0-100%) and for high multiplicity events (V0M:0-10%) are shown. In (b), the ratios for the p_{T}-spectra obtained from high multiplicity events (V0M:0-10%) with low spherocity $S_O < 0.47$ and high spherocity $S_O > 0.76$ are shown.

In Figure 6.2.2, the ratio for high multiplicity events (V0M:0-10%) is compared to the ratios for high and low spherocity events.

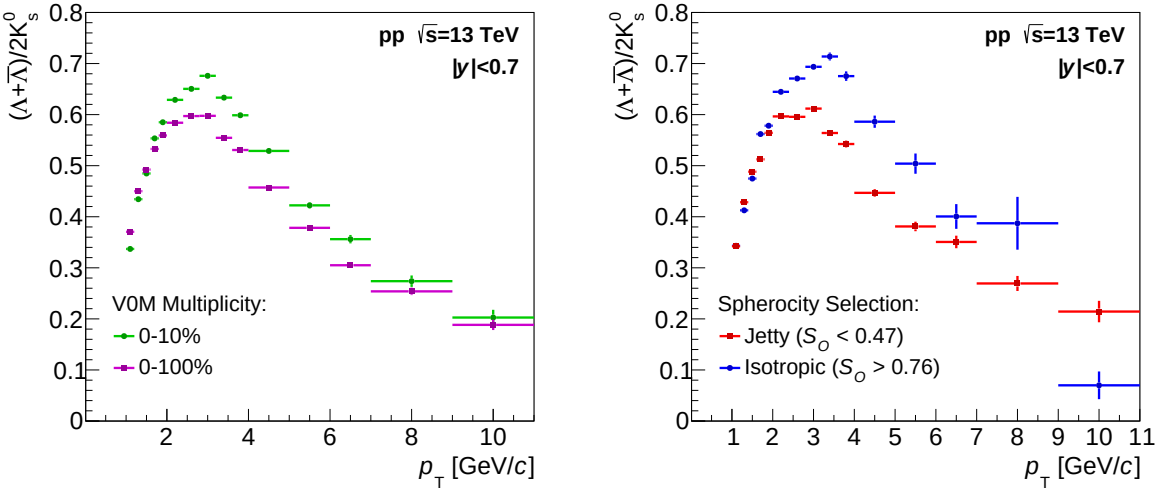

(a) (b)

Figure 6.2.1: The baryon-to-meson ratios $(\Lambda + \bar{\Lambda})/2K^0_s$ for events with no multiplicity bias (V0M:0-100%) and for high multiplicity events (V0M:0-10%) are shown in (a). The ratios for high multiplicity events (V0M:0-10%) with two additional spherocity cuts are shown in (b).

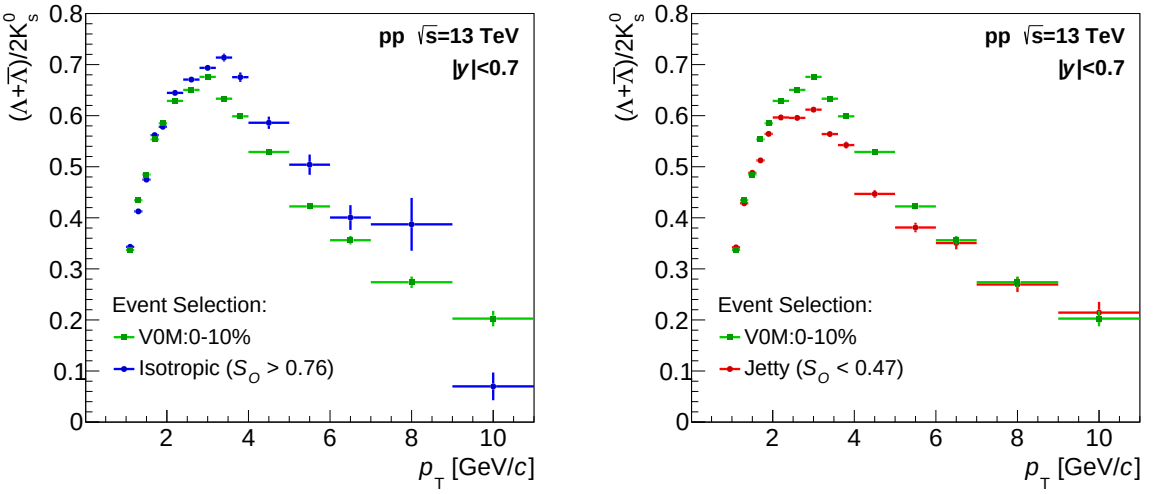

(a) (b)

Figure 6.2.2: The baryon-to-meson ratios $(\Lambda + \bar{\Lambda})/2K^0_s$ for high multiplicity events (V0M:0-10%) and for high spherocity events are shown in (a). The ratios for high multiplicity events (V0M:0-10%) and for high spherocity events are shown in (b).

7 Discussion

The results presented in Chapter 6 will be discussed here. In Figure 6.1.1, 6.1.2, and 6.1.3, the multiplicity and event shape dependence of the identified particle spectra are shown. For all three identified hadrons K^0_s, Λ, and $\bar{\Lambda}$, the particle productions increase for high multiplicity events (V0M:0-10%) compared for events without multiplicity bias (V0M:0-100%). The increased production of the K^0_s, Λ, and $\bar{\Lambda}$ particles with increasing multiplicity in pp collisions agree with previous studies [28, 49].

The p_{T}-spectra for the event shape selections performed by the spherocity cuts, exhibit similar behavior for all three identified hadrons. At low p_{T}, the isotropic events demonstrate an abundance of strange hadrons compared to the other three event selections. However, this should not be interpreted as strangeness enhancement generated by a QGP medium. Low-p_{T} particles originate from soft QCD processes and when specifically asking for events where soft QCD dominates, the result should be an abundance of soft QCD particles. The particle production rate for isotropic events decreases more rapidly than for jetty events and this gives rise to a crossing point in the intermediate p_{T} range, $\sim$ 3 GeV/c for K^0_s and $\sim$ 3.5 GeV/c for Λ and $\bar{\Lambda}$. At this point, high-p_{T} particles originating from hard QCD processes such as jets start dominating the spectra. Therefore, the crossing point is expected if isotropic event are, to a certain degree, successfully separated from jetty events. Consequently, the isotropic events have significantly fewer high-p_{T} particles, which results in low statistics in the high-p_{T} part ($\gtrsim$ 4 GeV/c) of the spectra. This affects in particular the Λ and $\bar{\Lambda}$ spectra, which overall have lower statistics compared to K^0_s.

Figure 6.2.1 demonstrates the results of the baryon-to-meson ratio $(\Lambda + \bar{\Lambda})/2K^0_s$ for the four event selections. In 6.2.1(a), the ratio obtained from events from all multiplicity classes (V0M:0-100%) is compared to the ratio for high multiplicity events (V0M:0-10%), where the relative enhancement of baryons to mesons is most pronounced for high multiplicity events. The enhancement of the baryon production for the high multiplicity events compared to V0M:0-100% events, can be observed predominantly in the intermediate range $2 \lesssim p_{\mathrm{T}} \lesssim 5$ GeV/c where the ratio peaks at 3 GeV/c. The increase of the $(\Lambda + \bar{\Lambda})/2K^0_s$ ratio in high multiplicity pp collisions agrees with previous studies summarized in [27, 50] and for which some of the results are shown in Figure 3.2.2.

In Figure 6.2.1(b), the $(\Lambda + \bar{\Lambda})/2K^0_s$ ratios for the spherocity event selections are shown and further, the low and high spherocity event selection are compared to the high multiplicity events (V0M:0-10%) in Figure 6.2.2. The ratio for jetty events is reminiscent of the ratio for V0M:0-100% events, while the relative enhanced baryon-to-meson production for isotropic events, with a pronounced peak at 3.5 GeV/c, exceeds the ratio result for high multiplicity events (V0M:0-10%). One interpretation of the relative increase of baryons compared to mesons in the range $2 \lesssim p_{\mathrm{T}} \lesssim 5$ GeV/c in high multiplicity pp collisions is strong radial flow being developed [51]. The radial flow pushes the abundant low-p_{T} (<2 GeV/c) particles towards higher p_{T}, where heavier hadrons are more affected than light hadrons. By using this interpretation on the ratios in Figure 6.2.2(a), the Λ and $\bar{\Lambda}$ particles are more effectively pushed towards higher p_{T} than K^0_s particles, with approximately half the mass of Λ. In isotropic events, where soft QCD processes dominates, the abundance of low-p_{T} particles give rise to a

stronger enhancement of the baryon-to-meson ratio than the ratio for the high multiplicity events. For the ratio comparison in Figure 6.2.2(b), the jetty events do not have a particle abundance in the low-p_T part of the spectra and therefore, do exhibit the same ratio enhancement observed in the high multiplicity events.

8 Conclusion and Outlook

The aim of this thesis was to study the multiplicity and event shape dependence of the identified K^0_s, Λ, and $\bar{\Lambda}$ productions in pp collisions and further, to examine if the results exhibit any heavy-ion like phenomena. The results for high multiplicity events (V0M:0-10%) and for events from all multiplicity classes (V0M:0-100%) were in agreement with previous studies. From the event shape analysis by spherocity cuts, the results indicate a successful separation of the events dominated by soft QCD processes from the events dominated by hard QCD processes. The results of the isotropic events exhibit reinforced high multiplicity behavior, i.e. the strange particle productions and the baryon-to-meson enhancement are further increased for isotropic events. The low-p_{T} particles in the isotropic events most plausibly originate from soft QCD processes, but whether or not this abundance is generated by a phenomenon similar to the collective behavior present in the hydrodynamical expansion of the QGP medium cannot be established by the results presented in this thesis.

In this thesis, the MC analysis was performed using PYTHIA. The event generator tends to underestimate the strangeness production in pp collisions and this underestimation grows with strangeness content. Since the decay of the multi-strange particle Ξ^- is the main contribution of secondary Λ particles, the feeddowns used as corrections for the Λ and $\bar{\Lambda}$ p_{T}-spectra are most certainty underestimated. This in turn gives the final Λ and $\bar{\Lambda}$ p_{T}-spectra large uncertainties. To improve the analysis performed in this thesis, a more valid feeddown is required. For an accurately estimated feeddown, the measured $\Xi^{\pm}$ spectra from real data are needed to correlate the p_{T} of the mother particle $\Xi^{\pm}$ into the p_{T} of the secondary $\Lambda(\bar{\Lambda})$. The accurate feeddown was not estimated in this thesis due to time limitations and instead, the feeddowns obtained from the MC analysis were used for removing the approximate fractions of secondary particles. To interpret the results of the spherocity analysis, a comparison of different MC event generators would have been a useful addition. By comparing the outcome for different models, a more elaborate theoretical interpretation may have been possible. Further, to truly establish the validity of the results presented in this thesis, systematic uncertainties have to be estimated and applied to the final results.

As a final note, if the heavy-ion like phenomena observed in small systems have the same origin as the QGP effects observed in large systems, then the QGP formation would no longer be a feature of extremely high temperatures and densities. Instead, the creation of the QGP in small systems would suggest it being a more general feature of hadronic collisions. This in turn would allow the dynamics of QCD being studied in large and small systems on the same terms.

Appendix A TPC PID Selection Cut for $\bar{\Lambda}$

The effects when applying the TPC PID cut of $\mid n\sigma_{\text{TPC}} \mid < 3$ on the yield of the $\bar{\Lambda}$ candidates are shown in Figure A.0.3. The MC analysis of the cut is demonstrated in (a) and (b). The MC analysis includes the yields from MC_{rec}^{blind}, with and without the cut, and the true yield from MC_{rec}^{PDG}. The effects of the TPC PID cut on real data are shown in (c) and (d).

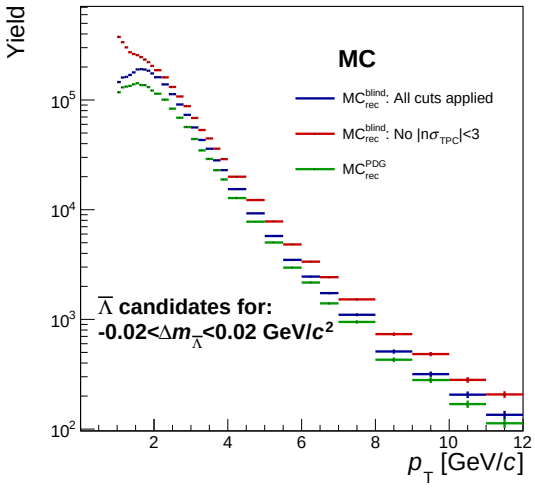

(a) The $\bar{\Lambda}$ yield from MC as function of p_{T}.

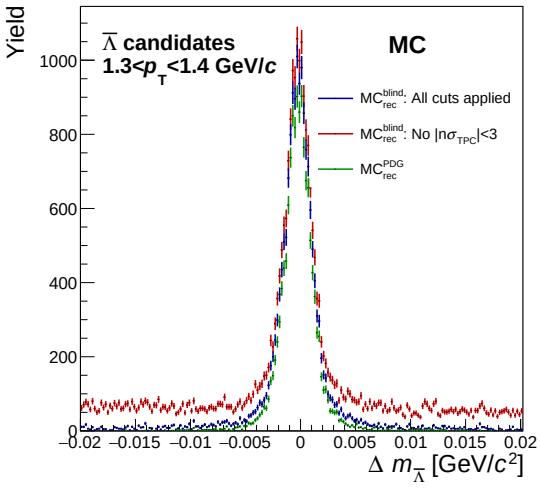

(b) The $\Delta m_{\bar{\Lambda}}$ distribution from MC in low p_{T}.

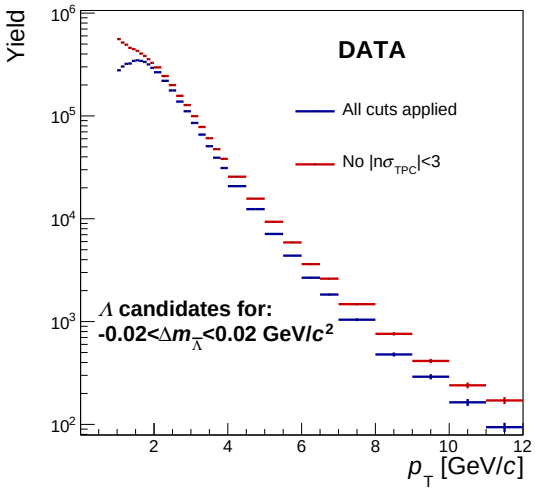

(c) The $\bar{\Lambda}$ yield from data as function of p_{T}.

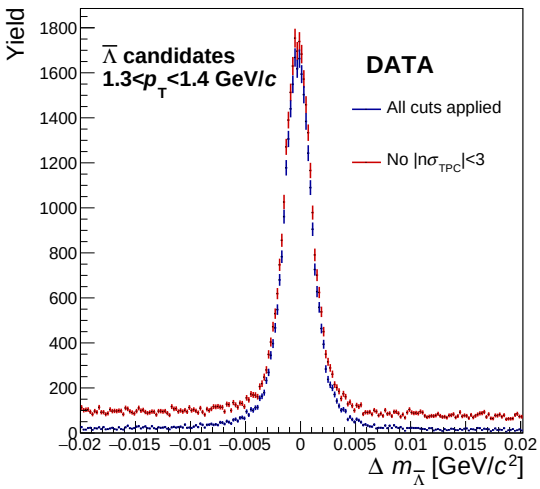

(d) The $\Delta m_{\bar{\Lambda}}$ distribution from data in low p_{T}.

Figure A.0.3: The figures (a) and (b) show the $\bar{\Lambda}$ yield from MC_{rec}^{blind} with all cuts applied (blue) and without the TPC PID cut of $\mid n\sigma_{\text{TPC}} \mid < 3$ (red). This is compared to the $\bar{\Lambda}$ yield from MC_{rec}^{PDG} (green). The figures (c) and (b) show $\bar{\Lambda}$ yield from data with all cuts applied (blue) and without the TPC PID cut (red). Both MC and data are for V0M:0-100%.

Bibliography

[1] L. H. Hoddeson, L. Brown, M. Riordan and M. Dresden. *The Rise of the standard model: Particle physics in the 1960s and 1970s*. Proceedings, Conference, Stanford, USA, June 24-27, 1992.

[2] G. Baym, Nucl. Phys. A **698**, XXIII (2002), [hep-ph/0104138].

[3] R. Pasechnik and M. Šumbera, Universe **3**, no. 1, 7 (2017), [arXiv:1611.01533 [hep-ph]].

[4] B. Abelev *et al.* [ALICE Collaboration], Phys. Lett. B **719**, 29 (2013) doi:10.1016/j.physletb.2013.01.012 [arXiv:1212.2001 [nucl-ex]].

[5] B. B. Abelev *et al.* [ALICE Collaboration], Phys. Lett. B **726**, 164 (2013) doi:10.1016/j.physletb.2013.08.024 [arXiv:1307.3237 [nucl-ex]].

[6] M. Aaboud *et al.* [ATLAS Collaboration], Phys. Rev. C **96**, no. 2, 024908 (2017) doi:10.1103/PhysRevC.96.024908 [arXiv:1609.06213 [nucl-ex]].

[7] P. Braun-Munzinger and J. Stachel, The quest for the quark-gluon plasma, Nature **448**, 302 (2007).

[8] M. Thomson, *Modern particle physics*, Cambridge University Press, New York, 2013.

[9] G. L. Kane, *Modern Elementary Particle Physics*, REDWOOD CITY, USA: ADDISON-WESLEY (1987) 344 P.

[10] B. R. Martin and G. Shaw, *Particle physics*, Chichester, UK: Wiley (2008) 442 p.

[11] C. Patrignani *et al.* (Particle Data Group), Chin. Phys. C **40**, no. 10, 100001 (2016) and 2017 update.

[12] A. K. Chaudhuri, A short course on Relativistic Heavy Ion Collisions, arXiv:1207.7028 [nucl-th]. (2012).

[13] W. Florowski. *Phenomenology of Ultra-Relativistic Heavy-Ion Collisions*. World Scientific Publishing; 2010.

[14] T. O. H. Richert, Λ/K^0_s associated with a jet in central Pb-Pb collisions at $\sqrt{s_{NN}}$ = 2.76 TeV measured with the ALICE detector, CERN-THESIS-2016-051.

[15] B. Muller, J. Schukraft and B. Wyslouch, Ann. Rev. Nucl. Part. Sci. **62**, 361 (2012) doi:10.1146/annurev-nucl-102711-094910 [arXiv:1202.3233 [hep-ex]].

[16] L. Li, N. Li and Y. Wu, J. Phys. G **40**, 075104 (2013) doi:10.1088/0954-3899/40/7/075104 [arXiv:1210.1658 [nucl-th]].

[17] R. Snellings, J. Phys. G **41**, no. 12, 124007 (2014) doi:10.1088/0954-3899/41/12/124007 [arXiv:1408.2532 [nucl-ex]].

[18] G. Torrieri, J. Phys. G **36**, 064007 (2009) doi:10.1088/0954-3899/36/6/064007 [arXiv:0901.0221 [nucl-th]].

[19] P. Koch, B. Müller and J. Rafelski, Int. J. Mod. Phys. A **32**, 1730024 (2017) doi:10.1142/S0217751X17300241 [arXiv:1708.08115 [nucl-th]].

[20] B. Muller, Acta Phys. Polon. B **43**, 761 (2012) doi:10.5506/APhysPolB.43.761 [arXiv:1112.5382 [nucl-th]].

[21] Ellipsix informatics, A smorgasboard of major experiment results, http://www.ellipsix.net/blog/2012/08/a-smorgasboard-of-major-experiment-results.html. [2017-11-07]

[22] G. Agakishiev *et al.* [STAR Collaboration], Phys. Rev. Lett. **108**, 072301 (2012) doi:10.1103/PhysRevLett.108.072301 [arXiv:1107.2955 [nucl-ex]].

[23] J. Adams *et al.* [STAR and STAR RICH Collaborations], nucl-ex/0601042.

[24] B. B. Abelev *et al.* [ALICE Collaboration], Phys. Rev. Lett. **111**, 222301 (2013) doi:10.1103/PhysRevLett.111.222301 [arXiv:1307.5530 [nucl-ex]].

[25] B. B. Abelev *et al.* [ALICE Collaboration], Phys. Lett. B **736**, 196 (2014) doi:10.1016/j.physletb.2014.07.011 [arXiv:1401.1250 [nucl-ex]].

[26] B. B. Abelev *et al.* [ALICE Collaboration], Phys. Rev. C **91**, 024609 (2015) doi:10.1103/PhysRevC.91.024609 [arXiv:1404.0495 [nucl-ex]].

[27] P. Foka and M. A. Janik, Rev. Phys. **1**, 154 (2016) doi:10.1016/j.revip.2016.11.002 [arXiv:1702.07233 [hep-ex]].

[28] J. Adam *et al.* [ALICE Collaboration], Nature Phys. **13**, 535 (2017) doi:10.1038/nphys4111 [arXiv:1606.07424 [nucl-ex]].

[29] B. B. Abelev *et al.* [ALICE Collaboration], Phys. Lett. B **727**, 371 (2013) doi:10.1016/j.physletb.2013.10.054 [arXiv:1307.1094 [nucl-ex]].

[30] A. Ortiz, G. Paić and E. Cuautle, Nucl. Phys. A **941**, 78 (2015) doi:10.1016/j.nuclphysa.2015.05.010 [arXiv:1503.03129 [hep-ph]].

[31] W. Barletta, M. Battaglia, M. Klute, M. Mangano, S. Prestemon, L. Rossi and P. Skands, arXiv:1310.0290 [physics.acc-ph].

[32] K. Aamodt *et al.* [ALICE Collaboration], JINST **3**, S08002 (2008). doi:10.1088/1748-0221/3/08/S08002

[33] B. B. Abelev *et al.* [ALICE Collaboration], Performance of the ALICE Experiment at the CERN LHC, Int. J. Mod. Phys. A **29**, 1430044 (2014) doi:10.1142/S0217751X14300440 [arXiv:1402.4476 [nucl-ex]].

[34] J. Alme *et al.*, Nucl. Instrum. Meth. A **622**, 316 (2010) doi:10.1016/j.nima.2010.04.042 [arXiv:1001.1950 [physics.ins-det]].

[35] J. Adam *et al.* [ALICE Collaboration], Eur. Phys. J. C **75**, no. 5, 226 (2015) doi:10.1140/epjc/s10052-015-3422-9 [arXiv:1504.00024 [nucl-ex]].

[36] B. Alessandro *et al.*, JINST **5**, P02008 (2010) doi:10.1088/1748-0221/5/02/P02008 [arXiv:1001.2276 [nucl-ex]].

[37] E. Abbas *et al.* [ALICE Collaboration], JINST **8**, P10016 (2013) doi:10.1088/1748-0221/8/10/P10016 [arXiv:1306.3130 [nucl-ex]].

[38] K. Aamodt *et al.* [ALICE Collaboration], Phys. Rev. Lett. **106**, 032301 (2011) doi:10.1103/PhysRevLett.106.032301 [arXiv:1012.1657 [nucl-ex]].

[39] AliRoot: ALICE Off-Line Framework for Simulation, Reconstruction and Analysis, `http://aliceinfo.cern.ch/Offline`, [2017-11-20].

[40] I. Antcheva *et al.*, Comput. Phys. Commun. **180**, 2499 (2009) doi:10.1016/j.cpc.2009.08.005 [arXiv:1508.07749 [physics.data-an]].

[41] T. Sjostrand, doi:10.3204/DESY-PROC-2009-02/41 arXiv:0809.0303 [hep-ph].

[42] L. Garren, C.-J. Lin, S. Navas, P. Richardson, T. Sjöstrand and T. G. Trippe,

[43] K. Aamodt *et al.* [ALICE Collaboration], Eur. Phys. J. C **71**, 1594 (2011) doi:10.1140/epjc/s10052-011-1594-5 [arXiv:1012.3257 [hep-ex]].

[44] L. Hanratty [ALICE Collaboration], K^0_S & Λ Production in ALICE, J. Phys. Conf. Ser. **509**, 012091 (2014). doi:10.1088/1742-6596/509/1/012091

[45] F. Dettori [LHCb Collaboration], arXiv:0909.5596 [hep-ex].

[46] V. Khachatryan *et al.* [CMS Collaboration], JHEP **1105**, 064 (2011) doi:10.1007/JHEP05(2011)064 [arXiv:1102.4282 [hep-ex]].

[47] D. Elia [ALICE Collaboration], J. Phys. Conf. Ser. **455**, 012005 (2013). doi:10.1088/1742-6596/455/1/012005

[48] W. R. Leo, *Techniques for Nuclear and Particle Physics Experiments: A How to Approach*, Berlin, Germany: Springer (1987) 368 p

[49] V. Khachatryan *et al.* [CMS Collaboration], Phys. Lett. B **768**, 103 (2017) doi:10.1016/j.physletb.2017.01.075 [arXiv:1605.06699 [nucl-ex]].

[50] C. Loizides, Nucl. Phys. A **956**, 200 (2016) doi:10.1016/j.nuclphysa.2016.04.022 [arXiv:1602.09138 [nucl-ex]].

[51] T. Kalaydzhyan and E. Shuryak, Phys. Rev. C **91**, no. 5, 054913 (2015) doi:10.1103/PhysRevC.91.054913 [arXiv:1503.05213 [hep-ph]].